Seasonal Stratospheric Photochemistry on Uranus and Neptune

Julianne I. Moses[a], Leigh N. Fletcher[b], Thomas K. Greathouse[c], Glenn S. Orton[d], Vincent Hue[c]

[a]*Space Science Institute, 4750 Walnut Street, Suite 205, Boulder, CO 80301, USA*
[b]*Department of Physics and Astronomy, University of Leicester, University Road, Leicester, LE1 7RH, UK*
[c]*Southwest Research Institute, San Antonio, TX 78228, USA*
[d]*Jet Propulsion Laboratory, MS 183-501, Pasadena, CA 91109, USA*

Abstract

A time-variable 1D photochemical model is used to study the distribution of stratospheric hydrocarbons as a function of altitude, latitude, and season on Uranus and Neptune. The results for Neptune indicate that in the absence of stratospheric circulation or other meridional transport processes, the hydrocarbon abundances exhibit strong seasonal and meridional variations in the upper stratosphere, but that these variations become increasingly damped with depth due to increasing dynamical and chemical time scales. At high altitudes, hydrocarbon mixing ratios are typically largest where the solar insolation is the greatest, leading to strong hemispheric dichotomies between the summer-to-fall hemisphere and winter-to-spring hemisphere. At mbar pressures and deeper, slower chemistry and diffusion lead to latitude variations that become more symmetric about the equator. On Uranus, the stagnant, poorly mixed stratosphere confines methane and its photochemical products to higher pressures, where chemistry and diffusion time scales remain large. Seasonal variations in hydrocarbons are therefore predicted to be

more muted on Uranus, despite the planet's very large obliquity. Radiative-transfer simulations demonstrate that latitude variations in hydrocarbons on both planets are potentially observable with future JWST mid-infrared spectral imaging. Our seasonal model predictions for Neptune compare well with retrieved C_2H_2 and C_2H_6 abundances from spatially resolved ground-based observations (no such observations currently exist for Uranus), suggesting that stratospheric circulation — which was not included in these models — may have little influence on the large-scale meridional hydrocarbon distributions on Neptune, unlike the situation on Jupiter and Saturn.

1. Introduction

Infrared and ultraviolet observations reveal that the stratospheric composition of Uranus and Neptune is being altered by solar-driven photochemistry, despite the great distance of these planets from the Sun (see the reviews of Atreya et al., 1991; Bishop et al., 1995; Yung and DeMore, 1999). Methane photolysis by solar ultraviolet radiation triggers the production of acetylene (C_2H_2), ethylene (C_2H_4), ethane (C_2H_6), methylacetylene (CH_3C_2H), diacetylene (C_4H_2), and other complex hydrocarbons, many of which have been observed on Uranus and Neptune (see Burgdorf et al., 2006; Orton et al., 2014c, and references therein). These photochemically produced species are radiatively active at mid-infrared wavelengths and can affect many aspects of the planetary atmosphere, such as its thermal structure, aerosol struc-

2

ture, energy balance, dynamical motions, and ionospheric structure. A full understanding of the three-dimensional (3D) time-variable behavior of photochemically produced species is therefore important for understanding many aspects of atmospheric physics and chemistry on Uranus and Neptune.

The non-zero obliquity (axial tilt) of Uranus and Neptune results in a seasonal dependence of solar insolation (see Fig. 1) that affects the production and loss rates of photochemically active constituents. Uranus, with its extreme ∼97.8° obliquity and rotational pole nearly in line with its orbital plane, experiences very unusual seasons compared to other Solar-System planets. Averaged over a year, high latitudes on Uranus receive greater solar insolation than low latitudes (see Fig. 2). Much of the planet alternates between being almost fully illuminated and being in almost complete darkness for half a year at a time (with one year on Uranus being equal to 84 Earth years), creating an opportunity for dramatic changes in hydrocarbon production as a function of season. Neptune's more moderate 28.3° obliquity results in seasonal forcing similar to that on the Earth, Mars, and Saturn, with low latitudes receiving a greater annual average solar insolation than high latitudes. Thus, averaged over a year, hydrocarbon production rates on Neptune will be greater at low latitudes than high latitudes. Given that a Neptune year is 165 Earth years, the winter high-latitude regions on Neptune endure long periods of time without sunlight, and the reduction in photochemical production of stratospheric hydrocarbons during the long polar winter could potentially affect global hydrocarbon abundances and/or result in different meridional distributions of hydrocarbons than shorter-period planets with similar obliquities, such as Saturn.
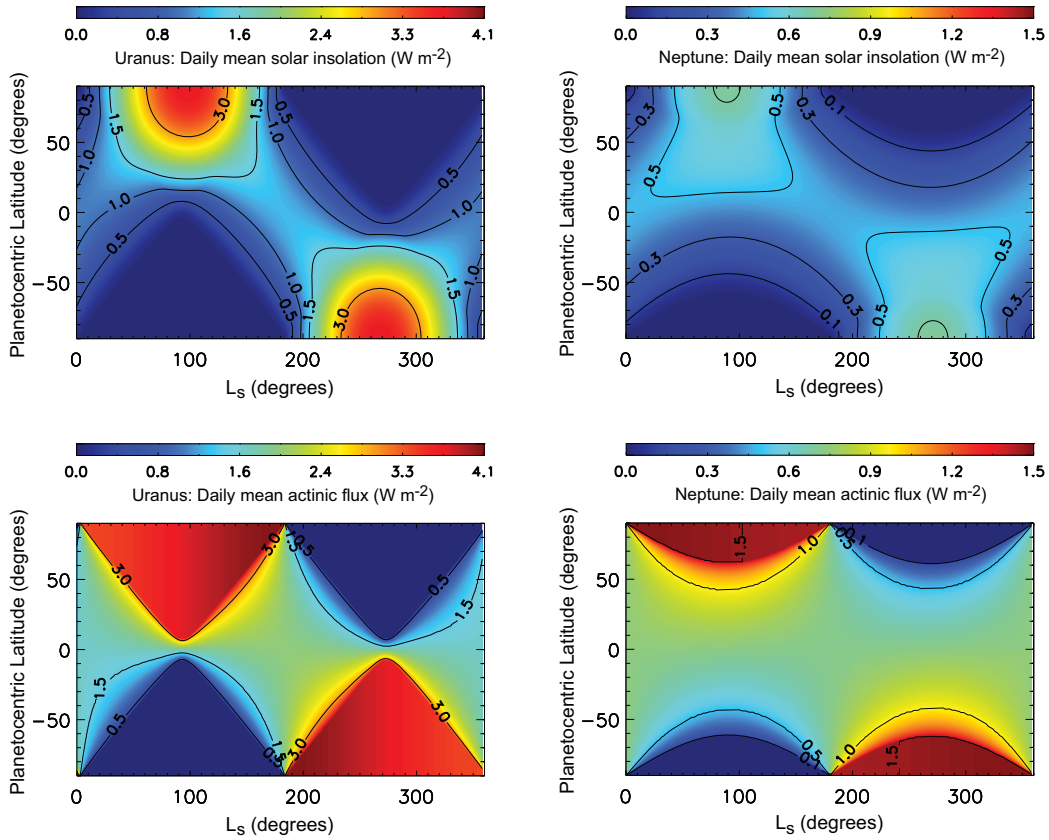
Figure 1: (Top) Mean daily solar insolation (W m^{-2} per planetary day) incident onto a unit horizontal surface at the top of the atmosphere of Uranus (Left) and Neptune (Right) as a function of planetocentric latitude and season, where season is represented by solar longitude L_s. (Bottom) Mean daily actinic flux (W m^{-2} per planetary day) at the top of the atmosphere of Uranus (Left) and Neptune (Right) as a function of planetocentric latitude and season. Note that a molecule being photodissociated does not care what direction the photon is coming from, just what the local photon flux is; therefore, the actinic flux, which is the solar flux without accounting for the cosine dependence of the solar zenith angle, is more relevant to the photochemistry discussion than the insolation at a "surface."
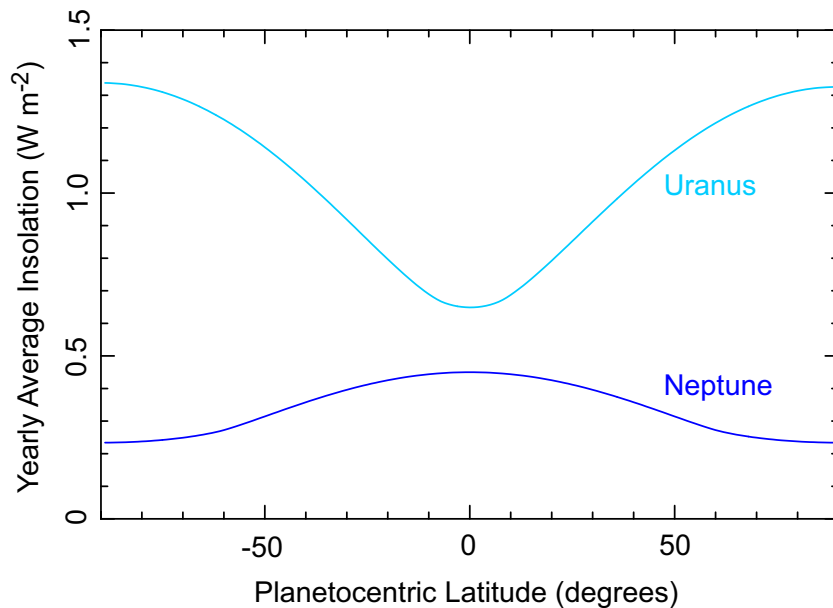
4

Figure 2: Annual average solar insolation at Uranus and Neptune as a function of latitude. Unlike the situation on other planets in the solar system, the polar regions of Uranus receive a higher annual average insolation than the equatorial region.

Although several one-dimensional (1D) photochemical models for Uranus and Neptune have been developed in the past (e.g., Atreya and Ponthieu, 1983; Romani and Atreya, 1988, 1989; Romani et al., 1993; Summers and Strobel, 1989; Bishop et al., 1990, 1992, 1998; Moses et al., 1992, 1995, 2005; Lellouch et al., 1994; Dobrijevic and Parisot, 1998; Dobrijevic et al., 2010; Bézard et al., 1999; Schulz et al., 1999; Orton et al., 2014c; Moses and Poppe, 2017), all previous models were designed for either global-average conditions or specific latitudes and times. Here, we present results from a 1D time-variable model that tracks the seasonal variation of photochemically produced hydrocarbons as a function of altitude for different latitudes. The models are similar to those of Moses and Greathouse (2005) in that the 1D

models for the different latitudes are not connected to each other via atmospheric circulation or any type of meridional transport, and the temperature structure is kept constant with latitude and time. Hue et al. (2015) show that for Saturn, the expected seasonal variations in stratospheric temperatures have only a minor influence on the abundances of the observable hydrocarbons, except in high-latitude regions during winter, where downward diffusion of hydrocarbons is faster as a result of atmospheric compression due to the lower temperatures. On the other hand, atmospheric dynamics can alter the vertical and meridional distribution of stratospheric constituents in potentially more significant ways. Comparisons of seasonal 1D photochemical models with the observed vertical and meridional distribution of hydrocarbon abundances can therefore provide useful information on the nature and strength of atmospheric dynamics, as well as atmospheric chemistry (see the Jupiter and Saturn studies of Moses and Greathouse, 2005; Liang et al., 2005; Nixon et al., 2007, 2010; Guerlet et al., 2009, 2010; Friedson and Moses, 2012; Sinclair et al., 2013, 2014; Zhang et al., 2013; Sylvestre et al., 2015; Fletcher et al., 2015, 2016; Hue et al., 2015, 2016; Moses et al., 2015).

We describe our photochemical models in section 2, present and discuss the results for the seasonal and meridional variations in hydrocarbons on Uranus and Neptune in section 3, compare the theoretical predictions with available observations in section 4, and discuss implications for future observations and modeling in section 5.

2. Photochemical model

The coupled set of continuity equations describing the vertical distribution of chemical constituents in the upper atmosphere of Uranus and Neptune is solved simultaneously by finite-difference methods, using the Caltech/JPL 1D KINETICS model (e.g., Allen et al., 1981; Yung et al., 1984). The Uranus model contains 181 vertical grid points, ranging from 5.6 bar to 1×10^{-8} mbar, with at least three grid points per scale height to ensure accuracy; the background temperature structure is taken from Orton et al. (2014b). The Neptune model contains 198 vertical grid points ranging from 5.0 bar to 1×10^{-8} mbar, with the background temperature structure taken from Moses et al. (2005), which was originally based on Orton et al. (1992), Roques et al. (1994), and Wang and Yelle (1992). There is no physically meaningful reason for the different number of grid points for each planet — the numbers were chosen simply to conform to previous models for these planets (Orton et al., 2014c; Moses and Poppe, 2017). Figure 3 shows the model temperature grid for both planets. Although the temperature-pressure profile is assumed to be constant with latitude, the altitude grid changes with latitude due to the variation of gravity with latitude and radius on a rapidly spinning, oblate planet (e.g., Lindal et al., 1985). Thirty different latitudes are considered, ranging from $-87°$ to $87°$ planetocentric latitude, every 6 degrees.

2.1. Chemistry inputs and boundary conditions

The chemical-kinetics inputs to the model are described in Moses et al. (2005, 2015) and references therein, with the complete updated reaction list presented in Moses and Poppe (2017). A total of $\sim$70 hydrocarbon and oxy-

7
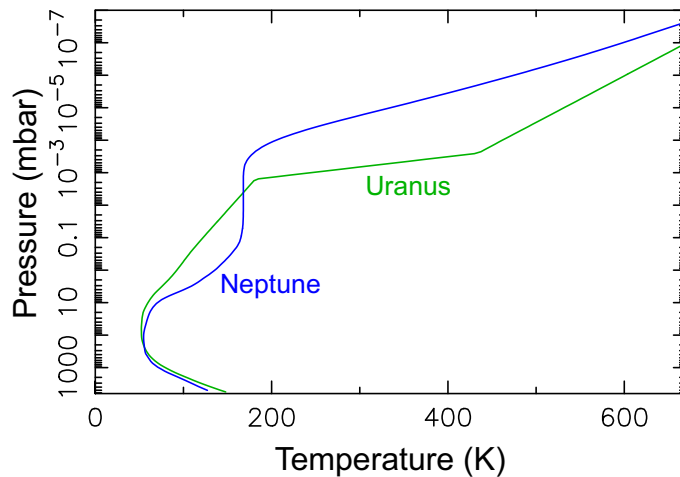
Figure 3: Temperature profiles for Uranus and Neptune (as labeled) adopted in the model.

gen species are considered, interacting through ∼500 chemical reactions, with 113 of these being photolysis reactions. The model includes condensation of C_2H_2, C_2H_6, C_3H_8, C_4H_2, C_4H_{10}, C_6H_6, H_2O, and CO_2, all of which will condense on both Uranus and Neptune (for the condensation procedure, see Moses et al., 2000b). Multiple Rayleigh scattering of the dominant gas-phase constituents is included, but aerosol scattering and absorption are not — the stratospheric aerosols are optically thin (Pollack et al., 1987; Moses et al., 1995; Karkoschka and Tomasko, 2009, 2011). The chemical production and loss rates and atmospheric transmission profiles are diurnally averaged, which is appropriate given that photolysis time scales and chemical time constants for the hydrocarbons are longer than a planetary day (∼17.24 hr rotation rate for Uranus, ∼16.11 hr for Neptune).

Methane from the deep atmosphere is the ultimate source of all carbon-bearing species in the model. Although methane condenses in the upper

8

troposphere of Uranus and Neptune, causing it to be depleted at higher altitudes, some CH_4 vapor makes it past the tropopause cold trap and into the stratosphere, just as water vapor does on the Earth. To streamline the current calculations, we neglect tropospheric methane condensation and instead fix the CH_4 volume mixing ratio at the lower boundary of the model to be representative of the value observed in the lower stratosphere — 1.6×10^{-5} for Uranus (based on Orton et al., 2014c) and 1.2×10^{-3} for Neptune (based on Fletcher et al., 2010; Lellouch et al., 2010, 2015). This assumption leads to an inaccurate methane profile in the troposphere and therefore inaccurate tropospheric hydrocarbon chemistry (which is relatively unimportant at these deeper altitudes, in any case), so the tropospheric results are ignored throughout the paper; only the stratospheric results are discussed. We also fix the mixing ratios of helium and CO at the lower boundary of the model. On Uranus, we assume the lower-boundary volume mixing ratio to be 15% for helium (Lindal et al., 1987) and 1.0×10^{-10} for CO (i.e., well below the upper limit of Teanby and Irwin, 2013). On Neptune, we assume the lower-boundary volume mixing ratio to be 19% for helium (Conrath et al., 1991b) and 8×10^{-8} (Luszcz-Cook and de Pater, 2013) for CO. The rest of the hydrocarbon and oxygen species are assumed to have concentration gradients of zero at the lower boundary, allowing the species to flow freely from their source regions at higher altitudes through the lower boundary at a maximum possible rate.

For the models presented here, we assume that the CH_4 mixing ratio at the base of the stratosphere is constant with latitude. Karkoschka and Tomasko (2009, 2011), Sromovsky et al. (2011, 2014), Irwin et al. (2012),

Tice et al. (2013), de Kleer et al. (2015), and Luszcz-Cook et al. (2016) provide observational evidence that the methane abundance in the troposphere varies with latitude on both Uranus and Neptune, with the polar regions being depleted in methane with respect to equatorial regions. The high-latitude depletion in CH_4 is particularly strong for Uranus. As discussed in the above references, these variations most likely arise from large-scale circulation patterns affecting the methane abundance in its condensation region in the upper troposphere, with CH_4 enhancements occurring in upwelling regions and depletions in downwelling regions, but the full details of this process have yet to be worked out. Moreover, it is currently unclear whether the latitude dependence extends into the stratosphere or not, or even how the methane is injected into the stratosphere in the first place. Does methane "leak" out of the troposphere into the stratosphere preferentially in regions where the tropopause is warmer and the local saturation vapor pressure higher (e.g., Orton et al., 2007), or is the methane dynamically injected into the stratosphere preferentially in regions with strong convective uplift (e.g., Karkoschka and Tomasko, 2011; Sromovsky et al., 2014; de Pater et al., 2014)? Given the lack of current information on the stratospheric behavior of methane as a function of latitude, our constant-with-latitude assumption provides a first-order look at the problem that can be altered when more data become available, such as with future observations from the *James Webb Space Telescope* (JWST) (Norwood et al., 2016). We do note, however, that when Greathouse et al. (2011) assumed a larger stratospheric methane abundance at the equator relative to the poles at Neptune, the temperature predictions from their radiative seasonal models were in closer agreement to

the observed temperatures, suggesting a latitude dependence of CH_4 in the stratosphere of Neptune, at least, is possible.

The oxygen-bearing species in our model are assumed to derive from external sources such as comets (Lellouch et al., 2005; Hesman et al., 2007; Luszcz-Cook and de Pater, 2013) or interplanetary dust (Moses 1992, Poppe 2016; see also Cavalié et al. 2014 & Moses and Poppe 2017), with CO having a possible significant internal source from the deeper troposphere (Fegley and Prinn, 1986; Lodders and Fegley, 1994; Fletcher et al., 2010; Luszcz-Cook and de Pater, 2013; Cavalié et al., 2017). Other major oxygen species from the interior, such as H_2O and CO_2, will condense at depth in the troposphere, with negligible amounts being transported into the stratosphere. To account for the external source of oxygen, we assume that H_2O, CO, and CO_2 are flowing in at the top of the atmosphere on both planets. The relative fluxes for these species are taken from Moses and Poppe (2017), who investigated the coupled oxygen-hydrocarbon photochemistry on Uranus and Neptune, and constrained the influx rates through comparisons of models with stratospheric observations of H_2O (Feuchtgruber et al., 1997, 1999; Lellouch et al., 2010), CO (Lellouch et al., 2005; Hesman et al., 2007; Fletcher et al., 2010; Luszcz-Cook and de Pater, 2013; Teanby and Irwin, 2013; Cavalié et al., 2014), and CO_2 (Feuchtgruber et al., 1999; Meadows et al., 2008; Orton et al., 2014c). For Uranus, these influx rates are 1.2×10^5 H_2O molecules cm^{-2} s^{-1}, 2.7×10^5 CO molecules cm^{-2} s^{-1}, and 2.8×10^3 CO_2 molecules cm^{-2} s^{-1} at the top boundary. For Neptune, the assumed influx rates are 2.0×10^5 H_2O molecules cm^{-2} s^{-1}, 2.0×10^8 CO molecules cm^{-2} s^{-1}, and 2.3×10^4 CO_2 molecules cm^{-2} s^{-1} at the top boundary.

Note that our assumption of a constant influx at the top boundary provides a reasonable approximation to the situation in which the oxygen is supplied by interplanetary dust particles, but the vertical profiles of the oxygen species would be more complicated if the bulk of the oxygen were supplied by a relatively recent large cometary impact, as has been suggested for Neptune in particular (see Lellouch et al., 2005; Hesman et al., 2007; Luszcz-Cook and de Pater, 2013; Moses and Poppe, 2017). We also assume a downward flux of atomic H at the upper boundary of both planets to account for an additional thermospheric source. We assume an influx rate of 5×10^7 and 1×10^7 H atoms cm^{-2} s^{-1}, respectively, at the top boundary of our Uranus and Neptune models based on Moses et al. (2005). All other species are assumed to have zero-flux boundary conditions at the top of the atmosphere.

2.2. Vertical transport and solar flux

As is typical in 1D photochemical models, vertical transport is assumed to operate through eddy and molecular diffusion. The eddy diffusion coefficient profile is one of the major free parameters for such models. Figure 4 shows the diffusion coefficients adopted in our models. For Uranus, we assume the vertical eddy diffusion coefficient $K_{zz} = 2430$ cm^2 s^{-1}, independent of altitude, based on Orton et al. (2014c). That assumption places the methane homopause at the $\sim 7 \times 10^{-2}$ mbar pressure level. For Neptune, we assume

$$K_{zz} = 10^5 \left(\frac{0.1}{P} \right)^{0.55}, \text{ for } P < 0.1 \text{ mbar}$$

$$= 10^5 \left(\frac{0.1}{P} \right)^{0.98}, \text{ for } 28 \text{ mbar} < P < 0.1 \text{ mbar}$$

$$= \quad 400, \text{ for } P > 28 \text{ mbar},$$

(1)

for K_{zz} in cm^2 s^{-1} and P in mbar, which places the methane homopause level at $\sim 8 \times 10^{-5}$ mbar. These eddy diffusion coefficient profiles were chosen in combination with our adopted lower-stratospheric CH$_4$ mixing ratio and our updated giant-planet chemical reaction list to provide a reasonable fit to the global-average stratospheric hydrocarbon abundances on both Uranus and Neptune (see Orton et al., 2014c; Moses and Poppe, 2017). For the nominal models presented here, the K_{zz} profile is assumed to be independent of latitude. The assumptions regarding the molecular diffusion coefficients are described in Moses et al. (2000a).
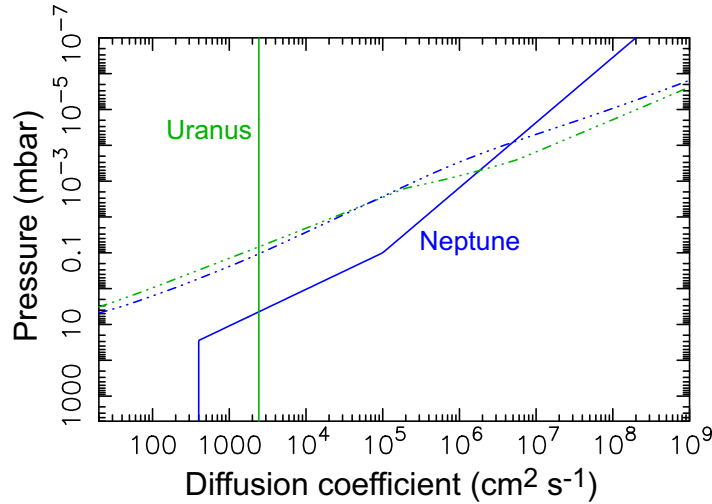

Figure 4: Profiles of the eddy diffusion coefficients (solid lines) and CH$_4$ molecular diffusion coefficients (dot-dashed lines) for Uranus (green) and Neptune (blue) adopted in the models.

For the solar ultraviolet flux, we take the average of the solar-cycle min-

13

imum and maximum fluxes presented in Woods and Rottman (2002). Although the hydrocarbon abundances at high altitudes are sensitive to the instantaneous solar flux, such that the solar-cycle variations should show up readily in the mixing ratio profiles in the upper stratosphere (e.g., Moses and Greathouse, 2005), chemical and transport time scales are much longer in the middle and lower stratosphere where the infrared observations are probing. Therefore, average solar flux values are sufficient for our purposes. We also include an isotropic source of stellar background UV radiation (taken from Mathis et al., 1983) and solar Lyman α photons that are being scattered from atomic hydrogen in the local interplanetary medium (LIPM). This LIPM source of photolyzing radiation is increasingly important to the photochemistry the farther the planet is located from the Sun, as was first demonstrated by Strobel et al. (1990) and Bishop et al. (1992). The LIPM source is needed particularly for the seasonal models presented here, as the scattered Lyman alpha provides a mechanism for CH_4 to be photolyzed even during the long polar winter on these planets, when high latitudes do not receive direct sunlight.

The magnitude of this LIPM source depends on both the solar cycle and heliocentric distance. Before the *Voyager* encounter with Neptune, the Ultraviolet Spectrometer (UVS) instrument recorded a background Lyman alpha LIPM intensity of roughly 340 Rayleighs (Broadfoot et al., 1989). Due to apparent calibration issues with the Voyager measurement (Gangopadhyay et al., 2005), we revise this value downward by a factor of $\sim$2, and based on modeling and observations (Gangopadhyay et al., 2005; Quémerais et al., 2009), we assume the intensity at Uranus is a factor of $\sim$1.3 larger than that

at Neptune. The actinitc flux from this LIPM source (assuming isotropic from the upper hemisphere only) is $2\pi \int_0^1 I(\tau, \mu)d\mu$, where I is the intensity incident on a small surface area with cosine of the incidence angle μ at vertical optical depth τ within the atmosphere. From Beer's law, $I(\tau, \mu) = I_0 \exp(-\tau/\mu)$, and the actinic flux becomes

$$F(\tau) = 2\pi I_0 \left(e^{-\tau} - \tau \left[-\mathrm{Ei}(-\tau) \right] \right), \tag{2}$$

where Ei is the exponential integral. In general, Lyman alpha photons from this LIPM source are absorbed at higher altitudes than the direct solar Lyman alpha source.

Unlike the case on Saturn, the small, faint ring systems of Uranus and Neptune do not cast sufficient shadows on the planets to notably affect the solar flux received and so are ignored in the calculations.

2.3. Seasonal model procedure

We first keep the season fixed at northern vernal equinox conditions (L_s = 0°) and run the 1D models for the different latitudes until steady-state solutions are achieved for that constant season. Then, we run the time-variable seasonal models with the above vernal equinox results as our initial conditions. The heliocentric distance and relevant solar zenith angle and flux calculations are updated every planetary day during the seasonal model runs. The planetary orbital positions as a function of time (and L_s) for two full planetary years are obtained from the JPL Horizons ephemeris calculator (Giorgini et al., 1996). The values for Uranus begin at $L_s = 0°$ in November, 1839 and end two planetary years later at $L_s = 0°$ in December, 2007; the

values for Neptune begin at $L_s = 0°$ in September, 1716 and end two planetary years later at $L_s = 0°$ in March, 2046. The full two-year time period was chosen originally to avoid any potential discontinuities due to the solar cycle being different at the beginning and end of the most recent planetary year when repeating the yearly calculations, but with the choice of solar-cycle averages, the full two-year sequence is unnecessary. By the same token, the results for a specific L_s for Neptune from this time period are relevant to the same L_s in the more recent era beyond 2007. Because the chemical species that are produced in the upper stratosphere can take thousands of years to diffuse down to the base of the model atmosphere, this two-planetary-year sequence is run again and again, with the results from the end of the second year being fed as initial conditions to the beginning of new two-year calculation, until a repeatable annual result is obtained. The Uranus model was iterated for a total of 80 Uranus years ($\sim$6721 Earth years), and the Neptune model for 10 Neptune years ($\sim$1648 Earth years) — more time is needed for the Uranus run because of the low eddy diffusion coefficient. The results from the converged solutions are presented below.

3. Results and Discussion

The photochemical product abundances vary with altitude, latitude, and time on Uranus and Neptune due to seasonal forcing (see full model output in the Supplementary Material). We begin by discussing the seasonal variations on Neptune, which are reasonably straightforward and qualitatively similar to those derived for Saturn (Moses and Greathouse, 2005; Hue et al., 2015). We then discuss seasonal variations on Uranus, which differ from those on

16

Neptune and Saturn — not only because of the planet's extreme axial tilt, but because of the very weak vertical mixing on Uranus. The results for both planets as a function of latitude are then presented, followed by the column densities as a function of both latitude and season.
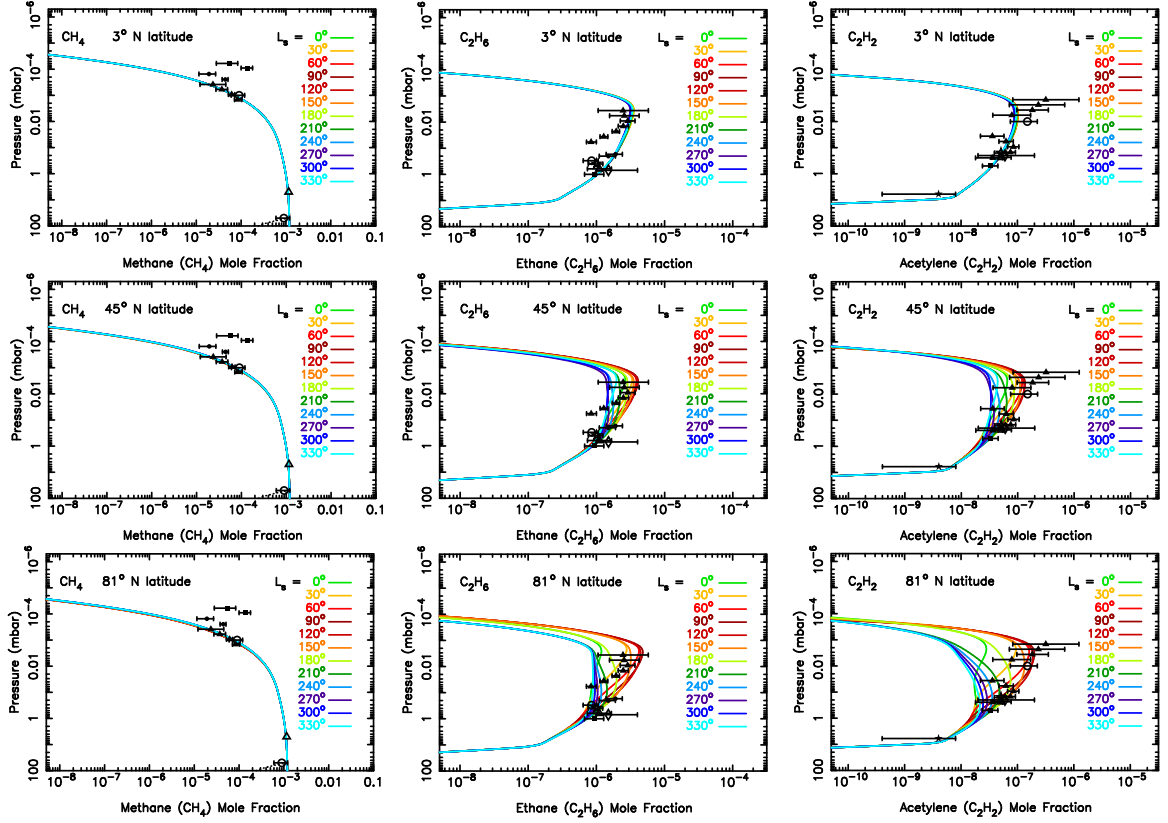
Figure 5: Mixing ratio profiles for key hydrocarbons (as labeled) on Neptune as a function of season for 3°N planetocentric latitude (Top), 45° planetocentric latitude (Middle), and 81° planetocentric latitude (Bottom). Seasons are shown every 30° in L_s. Data points are from various published observations (global average or low latitude, acquired during L_s = 230–300°) (Caldwell et al., 1988; Bézard et al., 1991; Bishop et al., 1992; Orton et al., 1992; Kostiuk et al., 1992; Yelle et al., 1993; Bézard et al., 1998; Schulz et al., 1999; Meadows et al., 2008; Fletcher et al., 2010; Greathouse et al., 2011; Lellouch et al., 2015), and unpublished Infrared Space Observatory hydrocarbon observations (Bruno Bézard, personal communication, 2001).
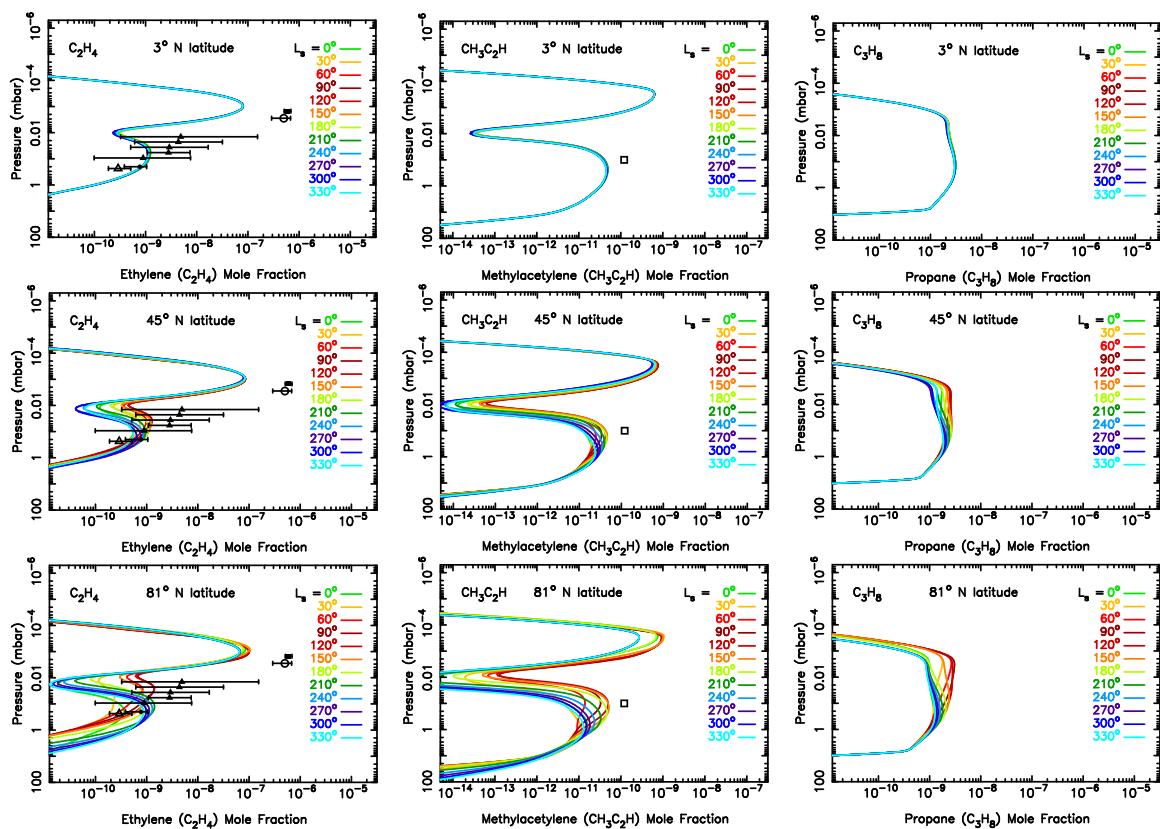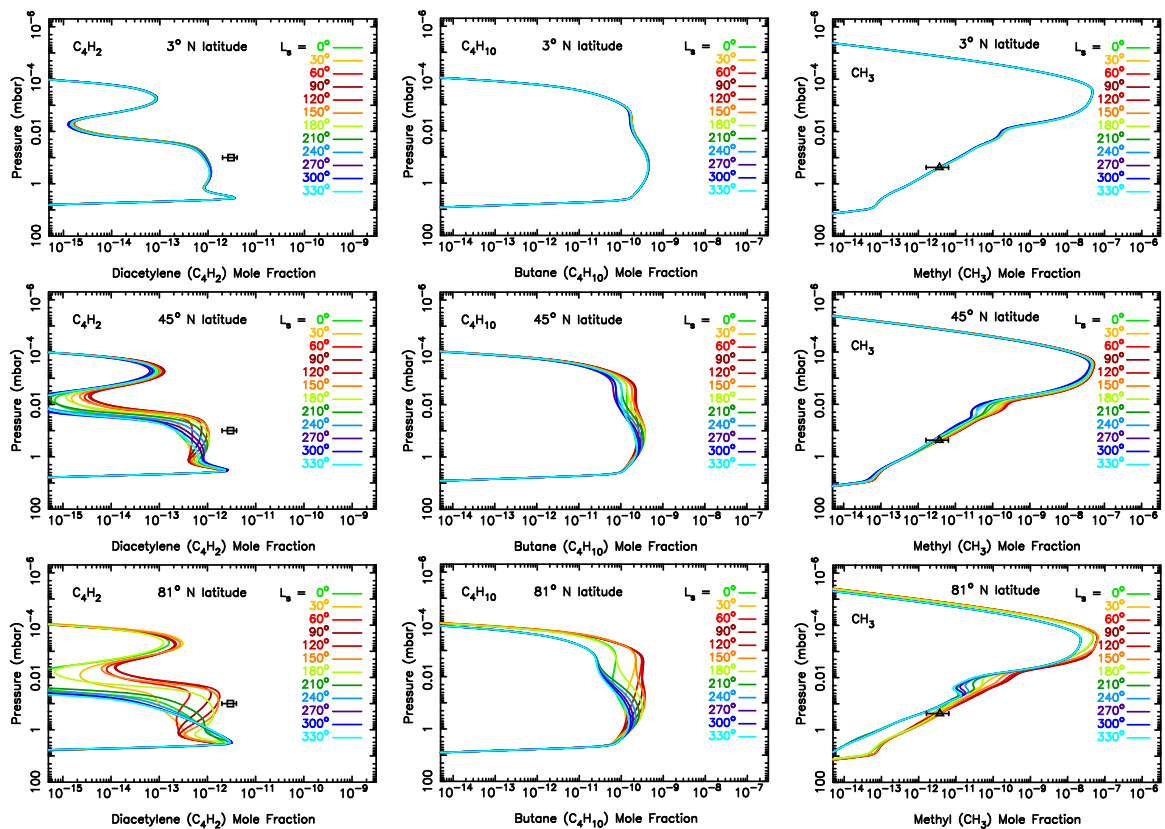
Fig. 5. *(continued)*.

19

Fig. 5. *(continued)*.

3.1. Seasonal variations in mixing ratios on Neptune

The vertical mixing-ratio profiles of several observed (or potentially observable) hydrocarbons on Neptune are shown in Fig. 5 as a function of season for representative low, middle, and high latitudes (top, middle, and bottom panels, respectively). Seasonal variations in the mixing ratios are apparent at altitudes above the few-millibar region for most of the photochemical products. Greater seasonal variation is exhibited at high latitudes than low latitudes, simply because the seasonal variation in solar insolation is greater at high latitudes than low latitudes (recall Fig. 1). Note that methane itself does not vary much with either season or latitude because its vertical profile is dominated by eddy and molecular diffusion rather than chemistry; the cumulative photochemical products do not rival the abundance of the parent CH_4 molecules, so photodestruction leads to only a very minor change in the mixing-ratio profile of methane.

For stable species with relatively long chemical lifetimes, such as C_2H_2 and C_2H_6, the seasonal variations are confined to high altitudes and become progressively smaller in magnitude at deeper pressures (see also Fig. 6). This behavior stems from the fact that both the diffusion time scales and chemical time constants for these species generally increase with increasing pressure (see Fig. 7, which displays the time constants at $-3°$ latitude for the vernal equinox situation at the start of the model run). Chemical time constants do vary considerably with both latitude and season, but the general trend of shorter time constants at higher altitudes holds true for all situations. Both the diffusion time scales and chemical lifetimes are less than a Neptune season in the region from ∼1 to a few μbar, where the C_2H_2 and C_2H_6 pro-
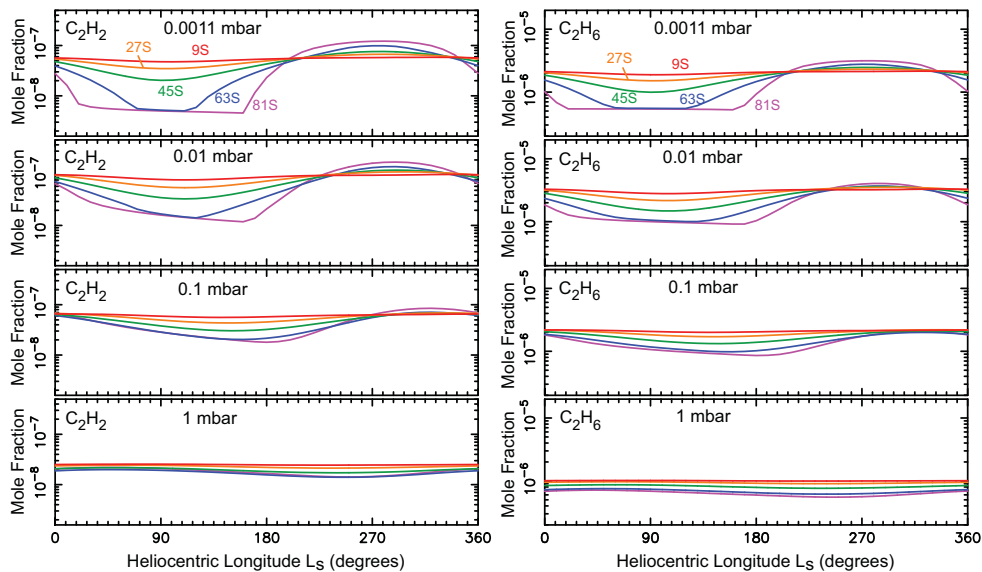
Figure 6: Mixing ratios of acetylene (left) and ethane (right) on Neptune as a function of season (represented by solar longitude L_s) at 1.1×10^{-3} mbar (top), 0.01 mbar (second from top), 0.1 mbar (third from top), and 1 mbar (bottom). Results are shown for five different latitudes: $-9°$ (red), $-27°$ (orange), $-45°$ (green), $-63°$ (blue), and $-81°$ (magenta). Seasonal variations are are prominent at lower pressures (higher altitudes) but become muted at higher pressures (lower altitudes), and are much greater at high latitudes than low latitudes. The 81° S latitude region receives no direct sunlight for an extended period during the winter, leading to a strong minimum during that period. Note also that the position of the minimum mixing ratio shifts to later in the year as the pressure increases in the atmosphere. (For interpretation of the references to color in this figure legend, the reader is referred to the online version of this article.)

duction rates peak in the upper stratosphere. Therefore, at ∼0.001 mbar, the C_2H_2 and C_2H_6 abundances respond quickly to changes in insolation. The increased insolation during the summer season leads to increased C_2H_2 and C_2H_6 production rates and an increased abundance of hydrocarbon photochemical products in general (see Figs. 5 & 6). The short vertical diffusion

time scales ensure that the photochemically produced species are transported rapidly to lower altitudes. Conversely, lower photochemical production rates in the winter lead to lower abundances of hydrocarbons at high altitudes, as the molecules produced in previous seasons have already been transported away. Photolysis by direct solar ultraviolet photons shuts off during the long polar winter, causing a strong dip in the high-altitude C_2H_2 and C_2H_6 abundances at high latitudes in the winter season (see Figs. 5 & 6), which quickly recovers as soon as the region receives direct sunlight again. However, solar Lyman α radiation scattered by H atoms in the local interplanetary medium continues to contribute to CH_4 photolysis even in the polar night, preventing a much stronger depletion in hydrocarbon abundances.

At 0.01 mbar, the chemical lifetime of C_2H_2 approaches a Neptune season and that of C_2H_6 exceeds a Neptune year (Fig. 7). The C_2H_2 and C_2H_6 mixing ratios in this pressure region are strongly influenced by molecules being transported into the region from higher altitudes, albeit with a time delay, which introduces a phase lag into the seasonal behavior. Seasonal variations are still apparent, but become more muted, and the minimum and maximum in the mixing ratios are shifted away from the solstices toward later times in the winter and summer seasons. Those phase lags continue to grow with depth, and the seasonal variations become reduced in magnitude, until almost no seasonal variations remain apparent in the few mbar region. At that point, the yearly averaged solar insolation controls the overall abundances, rather than the seasonally variable insolation. Other relatively chemically stable, long-lived species such as C_3H_8 and C_4H_{10} exhibit similar behavior as C_2H_2 and C_2H_6, with seasonal variations confined to higher altitudes, and
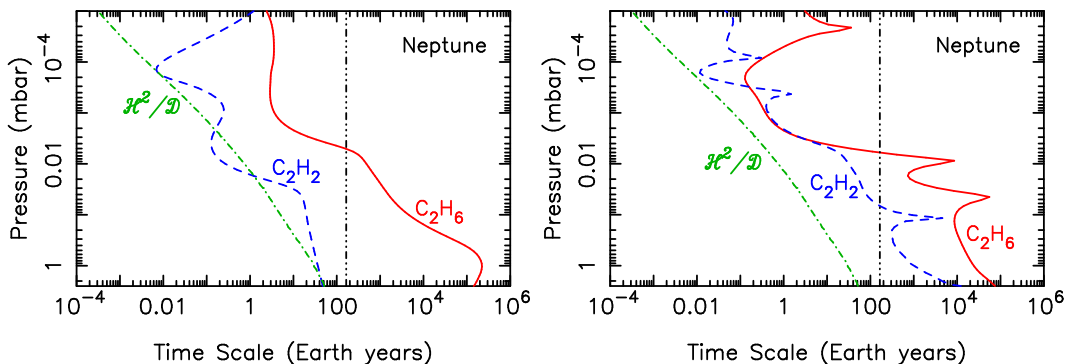
23

Figure 7: Time constants for photochemical loss (Left) and net photochemical lifetime (Right) above the condensation region on Neptune for C_2H_6 (red solid line) and C_2H_2 (blue dashed line), along with the diffusion time constant for C_2H_6 (green dot-dashed line, nearly identical to that for C_2H_2), compared to a Neptune year (vertical black triple-dot-dashed line) and a Neptune season (orange dotted line) for $-3°$ latitude, vernal equinox. The photochemical loss time scale is defined as the species concentration divided by the chemical loss rate; the net photochemical time scale is defined as the species concentration divided by the absolute magnitude of the chemical production rate minus the loss rate for the species. The latter gives a better measure of the species stability in the presence of efficient recycling processes; the sharp peaks occur where production and loss rates are nearly equal. The diffusion time scale is defined as the square of the generalized scale height divided by the generalized diffusion coefficient (see Moses and Greathouse, 2005). Note that chemical and diffusion time scales are shorter than a Neptune season in the peak production region from 1 to a few μbar but the net chemical lifetimes become longer than a Neptune season in the middle and lower stratosphere. (For interpretation of the references to color in this figure legend, the reader is referred to the online version of this article.)

phase lags introduced in the $\sim$0.01-10 mbar region.

Less stable species such as C_2H_4, CH_3C_2H, C_4H_2, and CH_3 that have shorter chemical lifetimes at depth continue to experience seasonal varia-

24

tions at all altitudes above their condensation regions (i.e., for the first three aforementioned species, which condense). The seasonal behavior of these species can be complicated, as both diffusion and *in situ* photochemistry affect the behavior, photodestruction of other seasonally variable species such as C_2H_2 and C_2H_6 contribute to their production, and photochemically produced radicals such as atomic H affect both production and destruction (see Moses et al., 2000a, 2005, 2015, for details). This more complicated chemistry (as well as uncertainties in the thermal structure for the observational abundance determinations) contributes to the apparent disagreements between the CH_3C_2H and C_4H_2 abundances predicted by the models and inferred from observations. The model-data mismatch for these species is not of great concern here, because each chemical rate coefficient in the model is subject to uncertainties, which when combined, lead to factors of a few uncertainties in the predicted abundances (e.g., Dobrijevic et al., 2003, 2010). Accounting for these uncertainties in our seasonal models is beyond the scope of this paper.

Full results for the abundances of all species in the model as a function of latitude and season can be found in the Supplementary Material for this article.

3.2. Seasonal variations in mixing ratios on Uranus

The mixing-ratio profiles for several observed (or potentially observable) hydrocarbons on Uranus are shown in Fig. 8 as a function of season for representative low, middle, and high latitudes. The first thing to note from Fig. 8 is that seasonal variations in hydrocarbon abundances are minor on Uranus compared to Neptune. Small changes in the C_2H_2 and C_2H_6 mixing

25

ratio with season are predicted in the $\sim$0.1–1 mbar region (see also Fig. 9), with virtually no seasonal change at deeper pressures. Vertical transport on Uranus is not very vigorous. The methane homopause is therefore located at a relatively deep $\sim 7 \times 10^{-2}$ mbar on Uranus — a pressure roughly three orders of magnitude greater than the homopause level on Neptune — and so the CH_4 is not carried as high up in the stratosphere on Uranus as it is on Neptune. Both C_2H_2 and C_2H_6 have their peak production region near $\sim$0.2 mbar on Uranus, at which point chemical time constants exceed (and diffusion time constants approach) a Uranus season (see Fig. 10). At altitudes above the 0.2-mbar level, the C_2H_2 production rate exceeds its loss rate, and because more C_2H_2 is produced in the summer season and less in the winter, the C_2H_2 mixing ratio at 0.1 mbar is greatest in the summer-to-fall time frame and least in the winter-to-spring, with the phase lag due to the long diffusion and chemistry time constants being apparent in Fig. 9. In contrast, the loss rate of C_2H_6 from photolysis exceeds the production rate at altitudes above the 0.2-mbar level, so more of the C_2H_6 that is being carried upward from its peak production region is destroyed in the summer than the winter, and the mixing ratio of C_2H_6 is greatest in the winter/spring and smallest in the summer/fall. At pressures of 1 mbar and greater, diffusion and chemical time constants are so long that no seasonal changes are expected for C_2H_2 and C_2H_6 at these pressures.
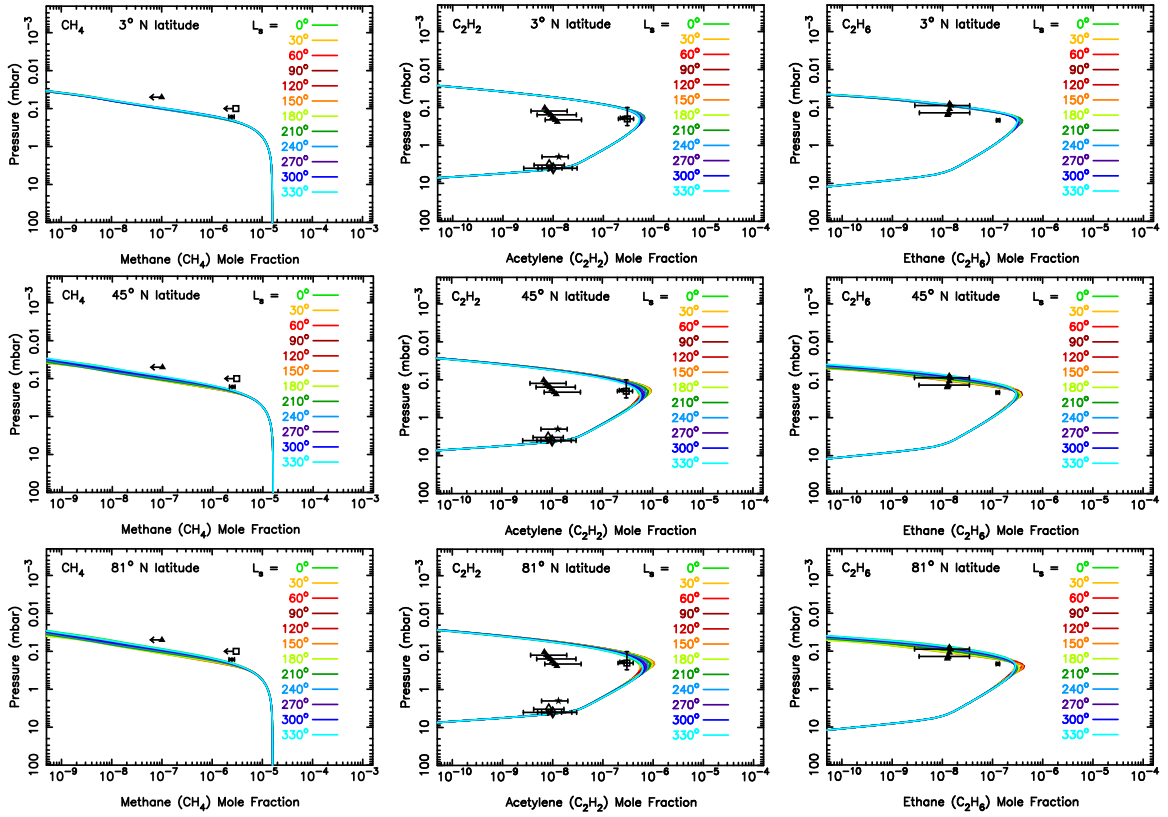
Figure 8: Mixing ratio profiles for key hydrocarbons (as labeled) on Uranus as a function of season for 3°N planetocentric latitude (Top), 45° planetocentric latitude (Middle), and 81° planetocentric latitude (Bottom). Seasons are shown every 30° in L_s. Data points are from various published observations (Encrenaz et al., 1986, 1998; Orton et al., 1987; Herbert et al., 1987; Caldwell et al., 1988; Yelle et al., 1989; Bishop et al., 1990; Bézard et al., 1999; Orton et al., 2014c).
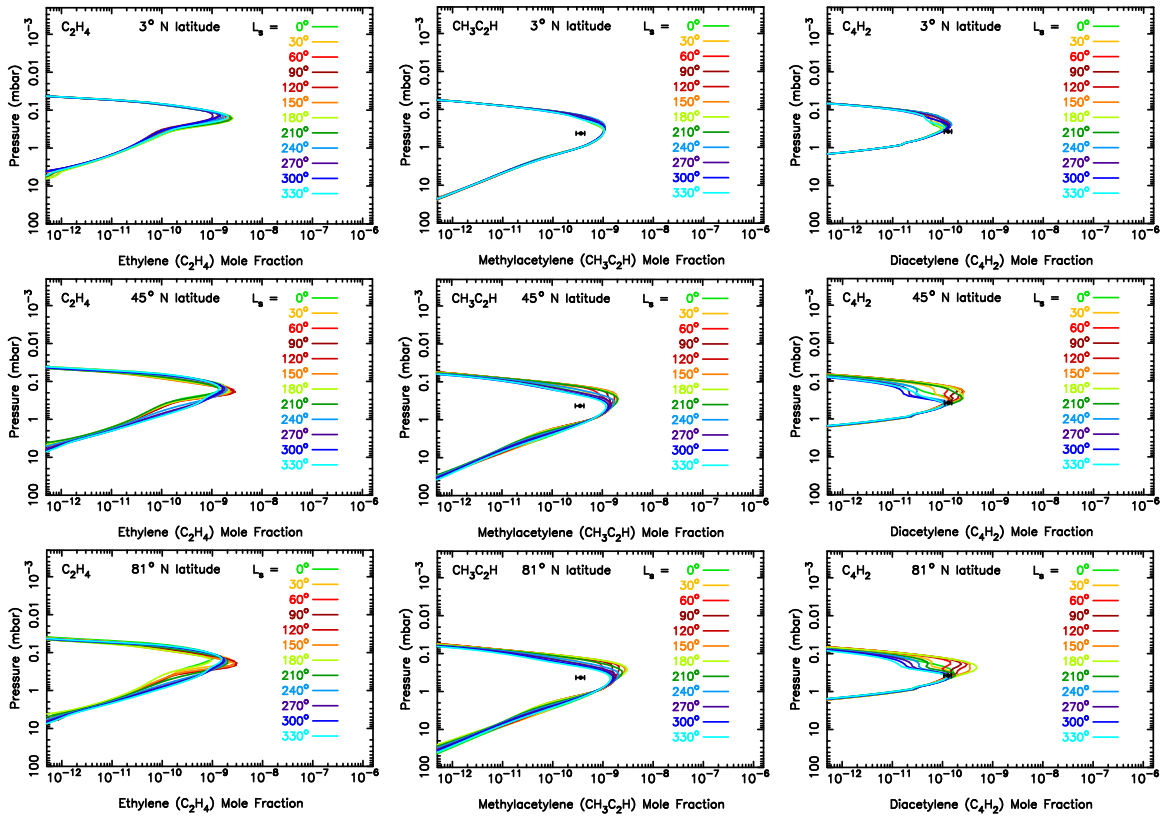
27

Fig. 8. *(continued).*

Even the species with shorter chemical lifetimes, such as C_2H_4 and CH_3C_2H experience relatively little seasonal variation in comparison with Neptune, because of the long diffusion time scales and lack of presence of these molecules at high altitudes where time scales are typically shorter. We would therefore not expect to observe much in the way of seasonal variations in hydrocarbon abundances on Uranus unless vertical transport — or stratospheric circulation in general — changes with season. One exception is C_4H_2, whose mixing ratio varies by as much as an order of magnitude in the $\sim$0.2–0.5 mbar region (see Fig. 8).
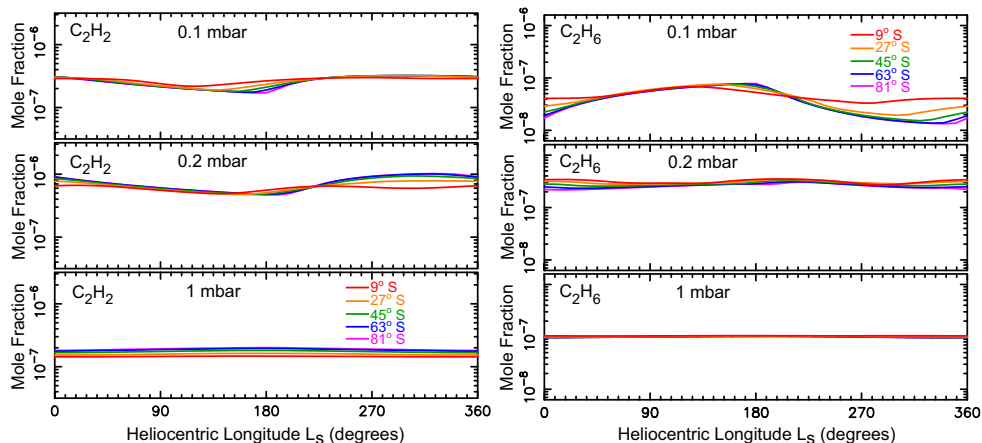
28

Figure 9: Mixing ratios of acetylene (left) and ethane (right) on Uranus as a function of season (represented by solar longitude L_s) at 0.1 mbar (top), 0.2 mbar (middle), and 1 mbar (bottom). Results are shown for five different latitudes: $-9°$ (red), $-27°$ (orange), $-45°$ (green), $-63°$ (blue), and $-81°$ (magenta). Seasonal variations are muted in general on Uranus but are more pronounced at lower pressures (higher altitudes). (For interpretation of the references to color in this figure legend, the reader is referred to the online version of this article.)

Note, however, that if stratospheric temperatures vary with season, the column abundance of all the condensable hydrocarbons will be greater at latitudes and seasons where the lower-stratospheric temperatures are warmer, because the available region over which the molecules can remain in the vapor phase expands to deeper pressures (i.e., the condensation region becomes more narrowly confined to the coldest pressure levels surrounding the tropopause). On Uranus, where the stratosphere is colder and the column density of hydrocarbons is so low anyway due to sluggish atmospheric mixing, changes in the pressure level of condensation due to seasonal temperature changes (e.g., Conrath et al., 1990) may have more of an effect on observed

29

hydrocarbon abundances than changes due to seasonal photochemistry itself. This effect applies to all hydrocarbons that can condense in the lower stratosphere, including C_2H_2 and C_2H_6, and would be observable if remote-sensing observations probe deep enough to sense the condensation region near the $\sim$1–10 mbar level.
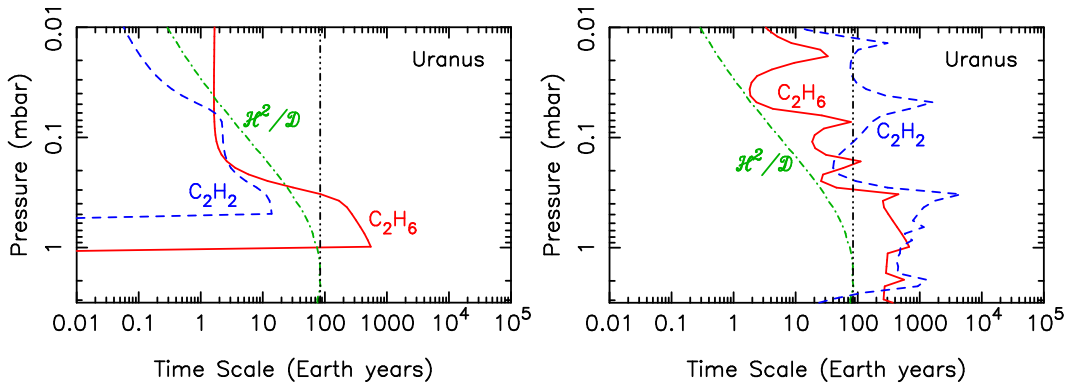

Figure 10: Time constants for photochemical loss (Left) and net photochemical lifetime (Right) above the condensation region on Uranus for C_2H_6 (red solid line) and C_2H_2 (blue dashed line), along with the diffusion time constant for C_2H_6 (green dot-dashed line, nearly identical to that for C_2H_2), compared to a Uranus year (vertical black triple-dot-dashed line) and a Uranus season (orange dotted line) for $-3°$ latitude, vernal equinox. (For interpretation of the references to color in this figure legend, the reader is referred to the online version of this article.)

3.3. Meridional variations in mixing ratios on Uranus and Neptune

As with seasonal variations, latitude variations in mixing ratios are more pronounced at higher altitudes. Fig. 11 illustrates how the C_2H_2, C_2H_6, CH_3C_2H, and C_4H_2 mixing ratios on Neptune vary as a function of latitude at four specific seasons: $L_s = 0°$ (dotted orange curves), $90°$ (solid blue curves), $180°$ (dashed green curves), and $270°$ (solid red curves). At high

altitudes (e.g., pressures less than $\sim$0.1 mbar), hemispheric dichotomies are readily apparent, typically with fewer photochemical products being present in the hemisphere experiencing winter and spring (due to the long accumulated time periods with low sunlight), and more photochemical products in the hemisphere experiencing summer and fall. At higher pressures, the mixing ratios of longer-lived species such as C_2H_2 and C_2H_6 become more symmetric about the equator, with the annual average actinic flux dominating the latitude variations (e.g., recall Fig. 2). On Neptune, the variations in annual average solar irradiation with latitude lead to a greater 1-mbar abundance of C_2H_2, C_2H_6, and CH_3C_2H at low latitudes in comparison with high latitudes, while species with short chemical lifetimes, such as C_4H_2, continue to exhibit hemispheric asymmetries at pressures of 1 mbar (see Fig. 11). Note also for the shorter-lived species that the increasing phase lag with depth can lead to hemispheric asymmetries at 1 mbar that are completely out of phase with those at 0.1 mbar. This effect is important to keep in mind when considering observations that are more sensitive to deeper levels — the abundances are out of phase at these depths in comparison to the instantaneous seasonal forcing, and the vertical profiles change significantly with season and latitude, which is important to keep in mind when choosing priors for retrievals.

The sluggish vertical mixing and large axial tilt on Uranus result in notable differences in latitude variations on Uranus (see Fig. 12), in comparison to Neptune. The longer vertical diffusion time scales and shorter year on Uranus result in seasonal variations being damped at 1 mbar on Uranus, and even species with relatively short photochemical lifetimes, like C_3H_4 and
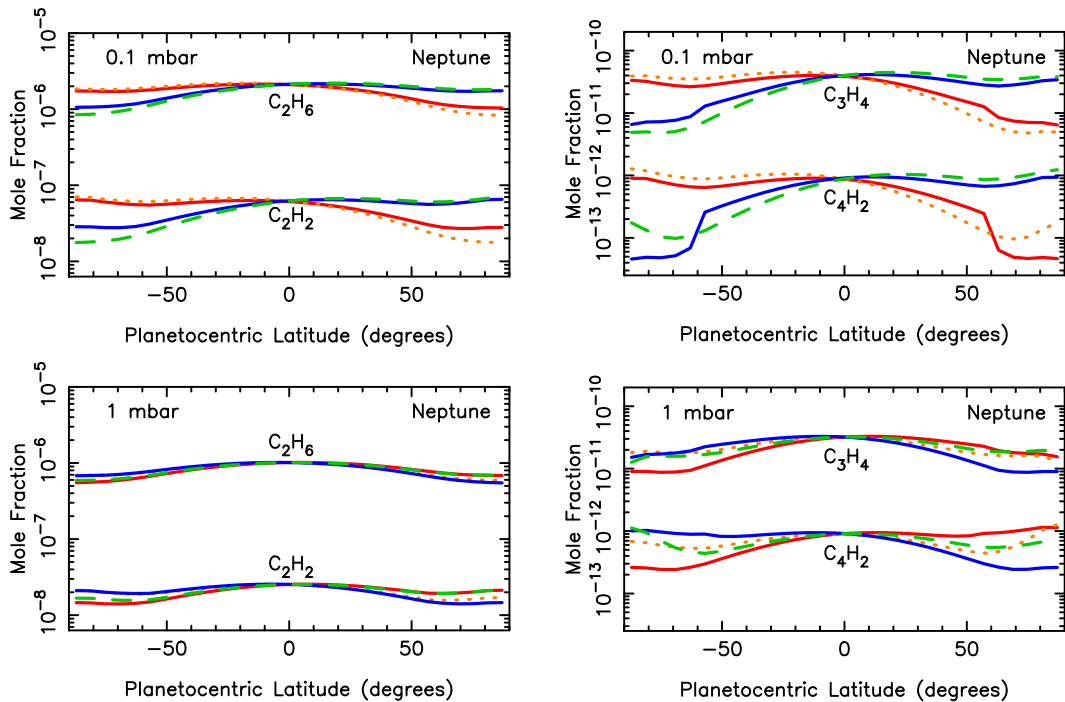
Figure 11: Mixing ratios of ethane and acetylene (Left) and methylacetylene and diacetylene (Right) at 0.1 mbar (Top) and 1 mbar (bottom) on Neptune for four different seasons: $L_s = 0°$ (dotted orange), 90° (solid blue), 180° (dashed green), and 270° (solid red). (For interpretation of the references to color in this figure legend, the reader is referred to the online version of this article.)

C_4H_2, are controlled by the annual average actinic flux at these pressures. Because the annual average daily insolation is greater at the poles than the equator on the highly tilted Uranus (Fig. 2), most photochemically produced species at 1 mbar have a larger mixing ratio at high latitudes than low latitudes. Ethane is an exception. The low-altitude homopause on Uranus results in different dominant hydrocarbon reactions in the region in which methane is photolyzed than on the other giant planets. Photolysis reactions control both the production and loss of ethane in the homopause region,

which act to counteract each other, and there are no effective in situ chemical loss processes for C_2H_6 at 1 mbar. The net column production rate for C_2H_6 therefore does not vary much as a function of latitude. The C_2H_6 that is produced near the homopause region diffuses downward, and because we have assumed that the eddy diffusion coefficient profile does not vary with latitude, the ethane abundance at depth on Uranus is relatively constant with latitude.
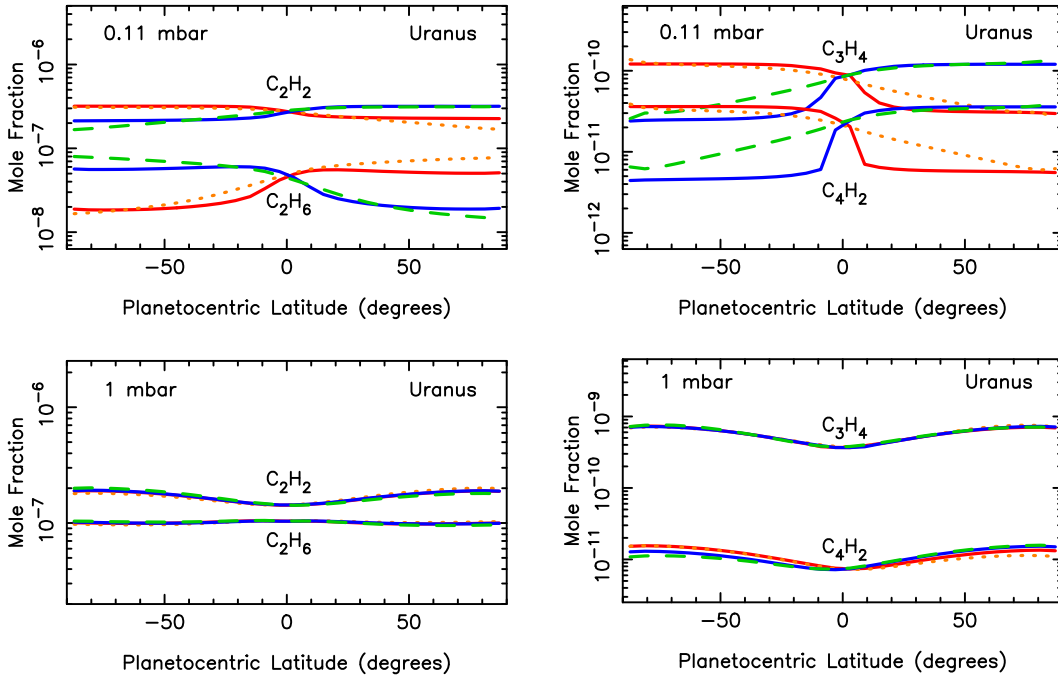

Figure 12: Same as Fig. 11, except for Uranus.

At higher altitudes on Uranus (e.g., 0.1 mbar in Fig. 12), the photochemically produced species exhibit hemispheric dichotomies, with most species being more abundant in the summer-to-fall hemisphere than the winter-to-spring hemisphere, as on Neptune. However, C_2H_6 is again an exception.

At the CH_4 homopause on Uranus, CH_4 is less abundant than on the other giant planets and is less effective at shielding the C_2H_6 from photolysis. Seasonal variations in solar irradiation therefore lead to a reduction in the high-altitude C_2H_6 abundance in the summer/fall hemisphere in comparison with the winter/spring hemisphere.

Keep in mind that the models presented in this paper do not consider meridional circulation or differences in vertical transport or methane abundance with latitude. Such processes could end up controlling latitude variations in photochemically produced species abundances on the giant planets, particularly on Uranus, where chemical and diffusion time constants are long and latitudinal/seasonal variations are predicted to be weak.

3.4. Variations in column abundance with latitude and season on Neptune

Because the hydrocarbon mixing ratios change significantly with altitude and the because the observed emission is proportional to the column abundance of the molecules when the emission lines are optically thin, it is convenient to consider the column abundance above various pressure regions when predicting observable changes as a function of latitude and time. Figs. 13–17 show how the column abundances of various hydrocarbons above different pressure levels vary as a function of latitude and season on Neptune.
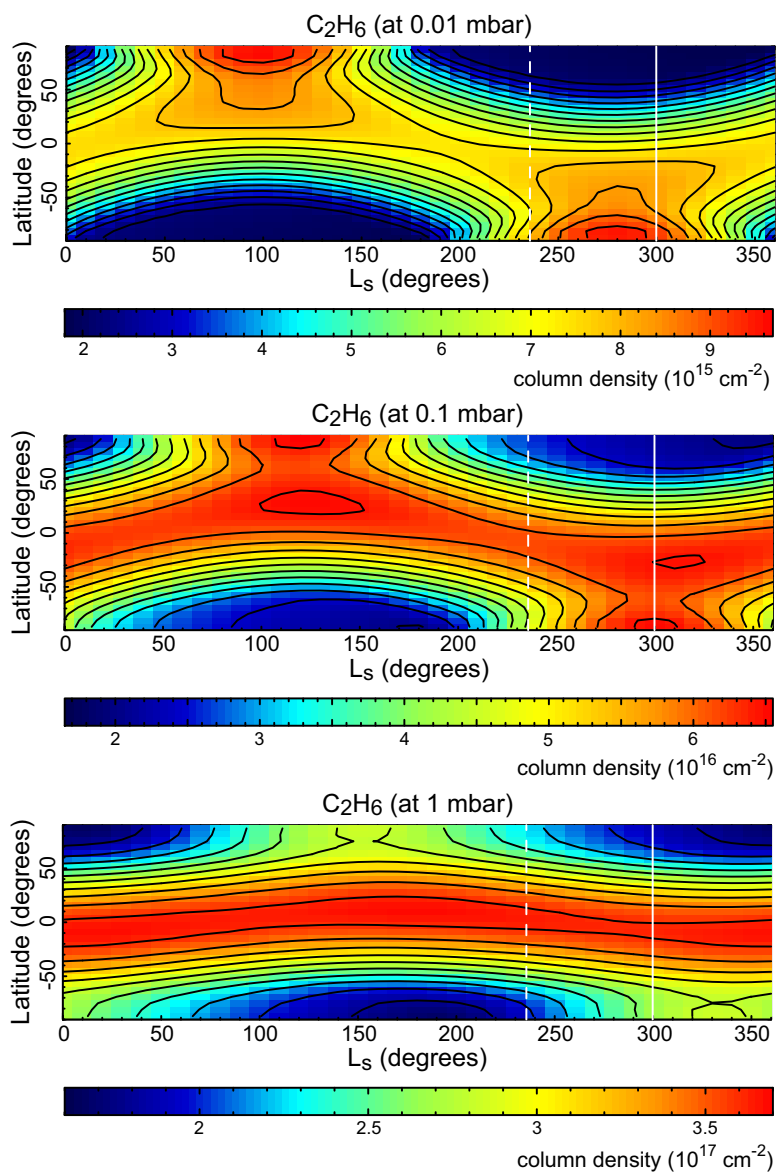
Figure 13: The column abundance of ethane on Neptune above 0.01 mbar (Top), 0.1 mbar (Middle), and 1 mbar (Bottom), as a function of planetocentric latitude and season (L_s). The dashed vertical line represents the time of the *Voyager* encounter, and the solid vertical line represents 7 September 2018, the date of the next Neptune opposition.
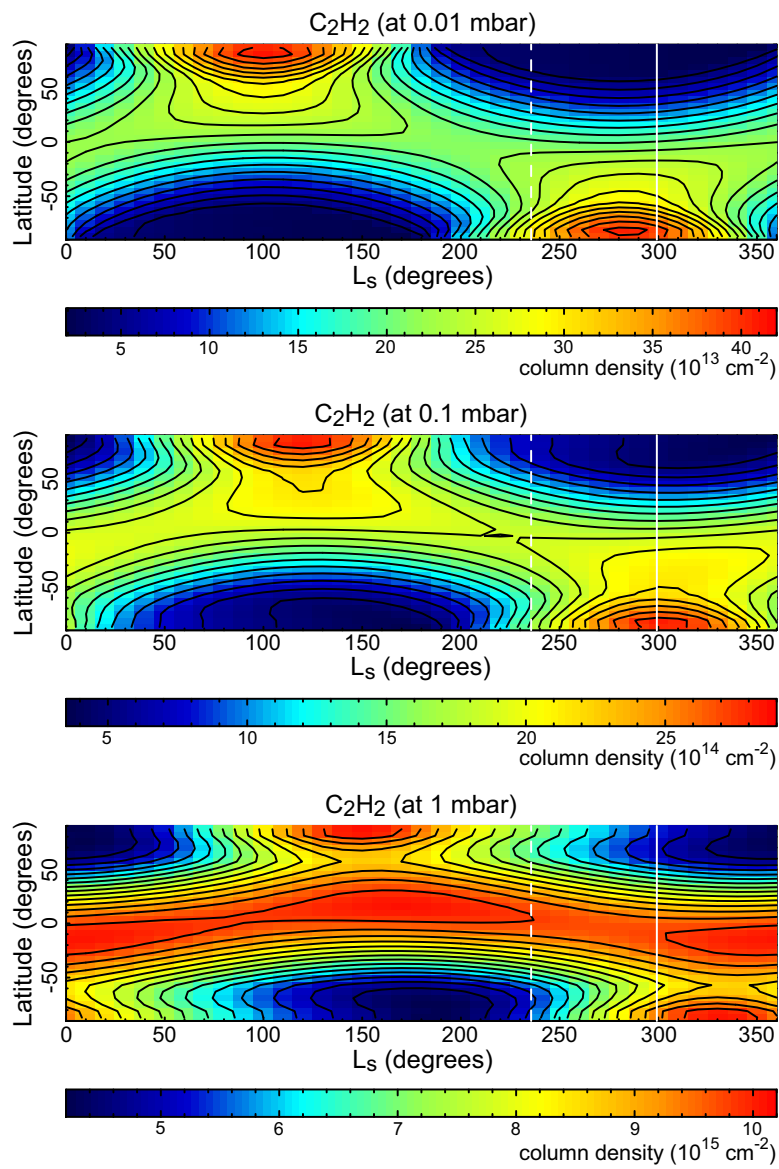
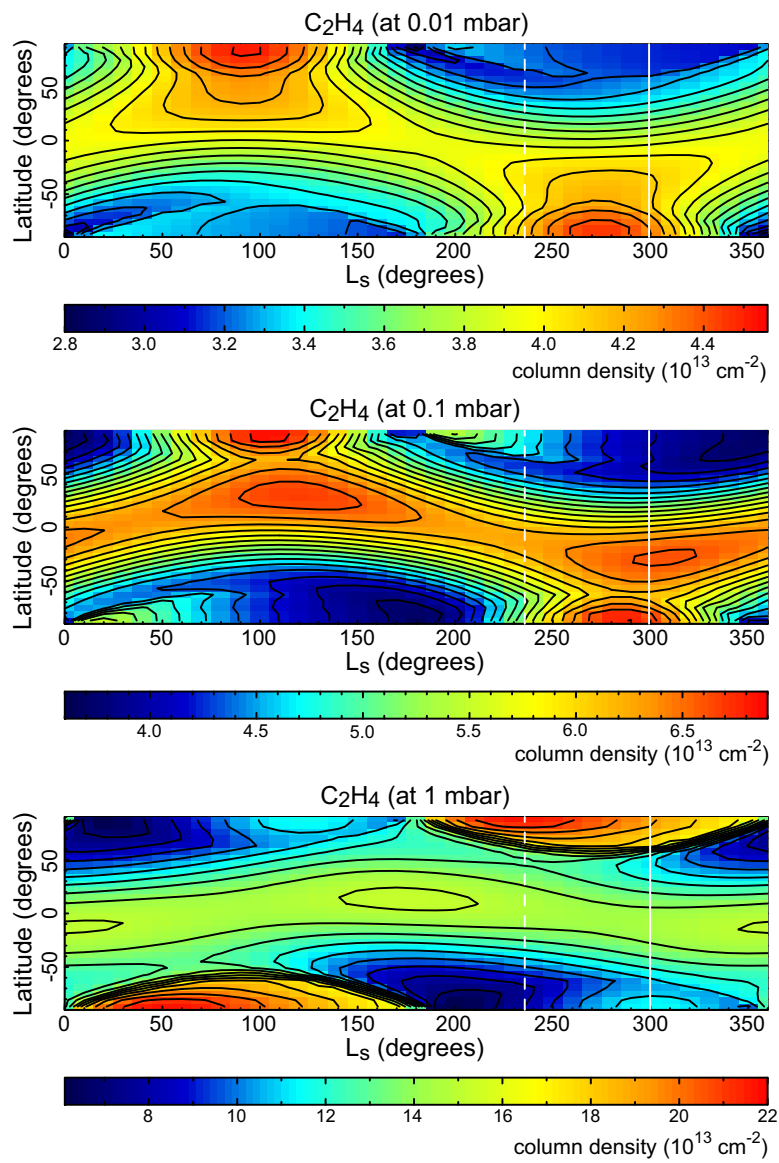Figure 14: Same as Fig. 13, except for acetylene.

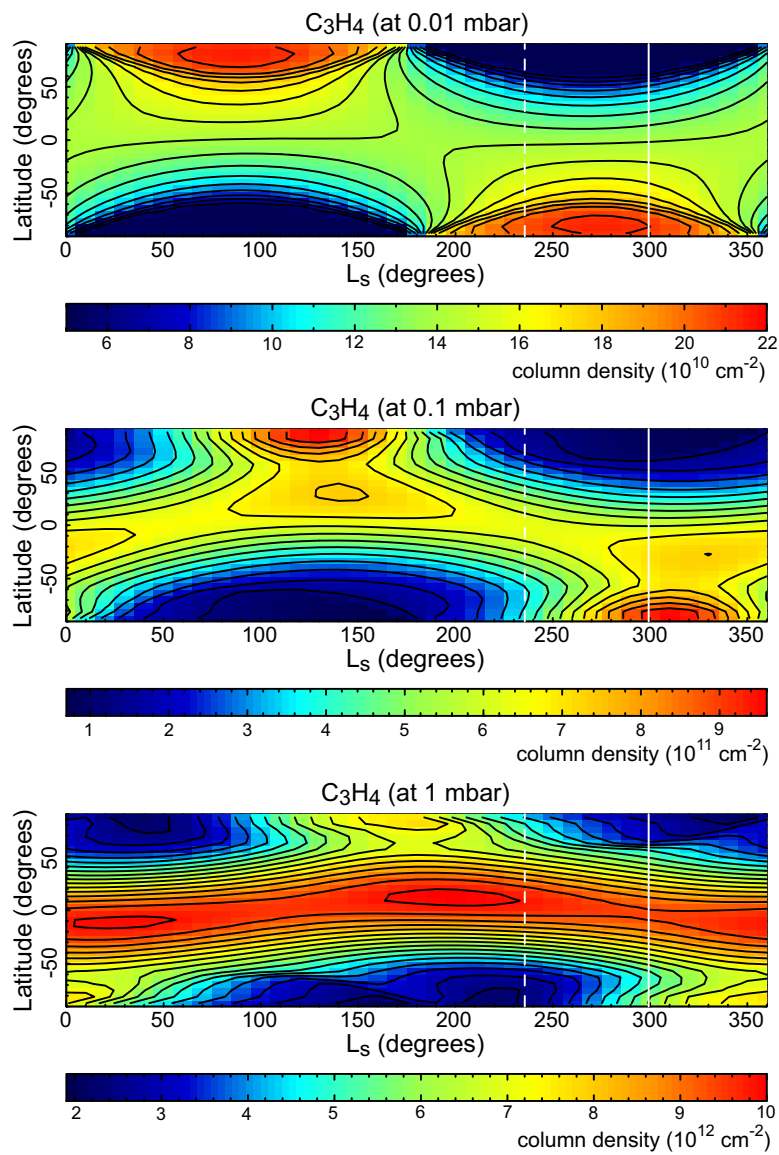Figure 15: Same as Fig. 13, except for ethylene.

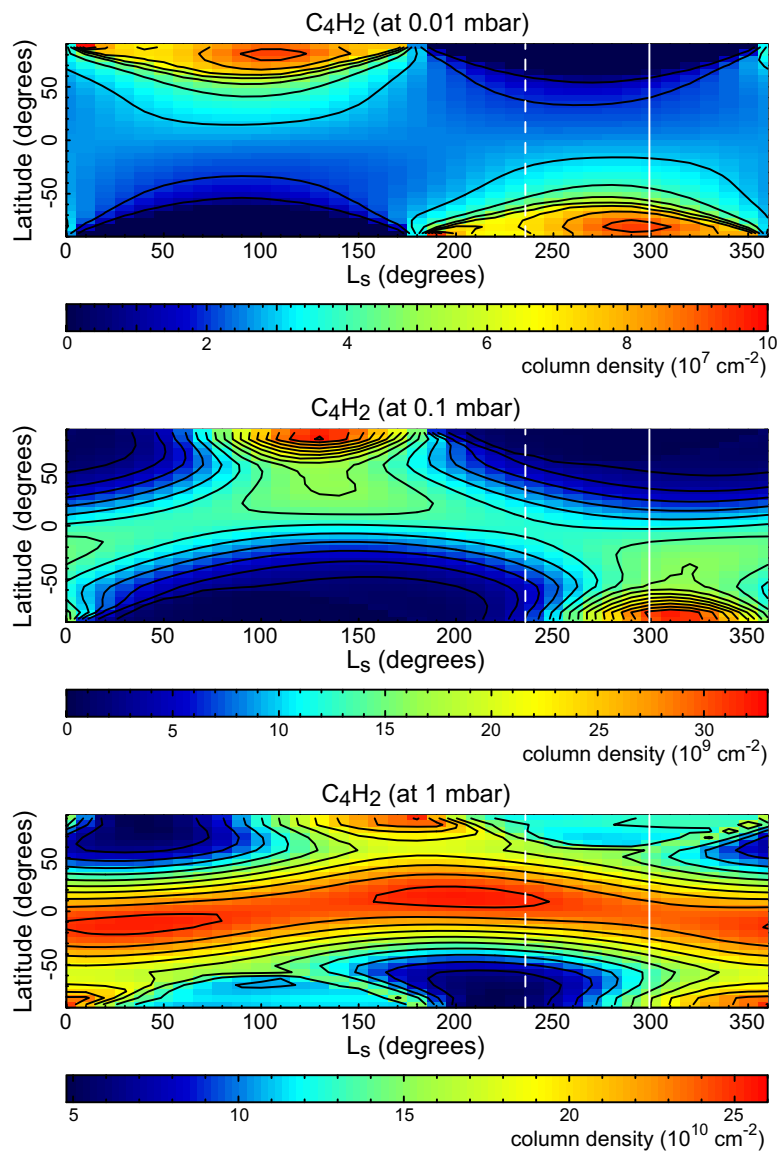Figure 16: Same as Fig. 13, except for methylacetylene.

Figure 17: Same as Fig. 13, except for diacetylene.

As was discussed in section 3.1, the abundances of most of the hydrocarbon photochemical products closely track the seasonal variation of solar insolation at high altitudes, causing the hydrocarbon column densities above 0.01 mbar to be much greater in the summer hemisphere in comparison to the winter hemisphere. However, chemical and diffusion time scales increase with depth in the atmosphere, leading to increasing phase lags in the abundance maxima and minima with depth at any particular latitude, along with meridional profiles of column abundance that become more symmetric about the equator at greater depths. These changes are readily apparent for C_2H_6 (Fig. 13), C_2H_2 (Fig. 14), and CH_3C_2H (Fig. 16).

Similar trends are seen for C_2H_4 (Fig. 15) and C_4H_2 (Fig. 17), although these two species also exhibit some additional interesting behavior. Note from Fig. 15 that the C_2H_4 column abundance above 1 mbar begins to increase strongly during the high-latitude winter months. This behavior results from the fact that photolysis is normally an effective loss process for C_2H_4 in the 0.1-10 mbar region, but direct solar UV photolysis is absent during the winter polar night. Although the stellar background UV source and scattered LIPM Lyman alpha photons are still available at that time, the overall C_2H_4 photolysis rate is greatly diminished, and the local production rate of C_2H_4 exceeds its loss rate. The dominant production of C_2H_4 at this time occurs through $C_2H_2 + H + M \rightarrow C_2H_3 + M$, followed by $C_2H_3 + H_2 \rightarrow C_2H_4 + H$, causing a net conversion of C_2H_2 into C_2H_4 during the long winter polar nights at $\sim$0.1-10 mbar. Diffusion of C_2H_4 from higher altitudes into this region also contributes to the increase. For C_4H_2, Fig. 17 illustrates that high-altitude production of C_4H_2 occurs most readily during the long

40

high-latitude summers, when the sun never sets, with much less production at other latitudes/times. The seasonal and meridional behavior at 1 mbar is more complicated and reflects the diffusion source from higher altitudes, with its associated phase lag, as well as in situ production and loss. One interesting feature that shows up in the C_4H_2 column density plot at 1 mbar is a brief local maximum as the sunlight returns to the high-latitude regions in the late winter or spring.

3.5. Variations in column abundance with latitude and season on Uranus

Figure 18 illustrates how the column abundances of several hydrocarbon photochemical products vary with latitude and season on Uranus. Because the hydrocarbons are vertically confined to deeper stratospheric levels due to the weak atmospheric mixing on Uranus, we do not show the results for multiple pressures, but instead plot the column abundance above 0.25 mbar, which is near the peak of the contribution function for most of the observed hydrocarbon bands in the *Spitzer*/IRS infrared observations (Orton et al., 2014b,c).

The column densities of C_2H_2, CH_3C_2H, and C_4H_2 exhibit maxima in the summer-to-fall hemispheres and minima in the winter-to-spring hemispheres, with strong hemispheric dichotomies apparent during most seasons. As with Neptune, this result is caused by the greater photochemical production rates during periods and locations with higher mean daily solar insolation, combined with a phase lag due to the diffusion of hydrocarbons from higher altitudes. Unlike Neptune, however, these species do not have a maximum column abundance near the equator when averaged over a year, as can be seen from the generally low column abundances in the equatorial region.

41
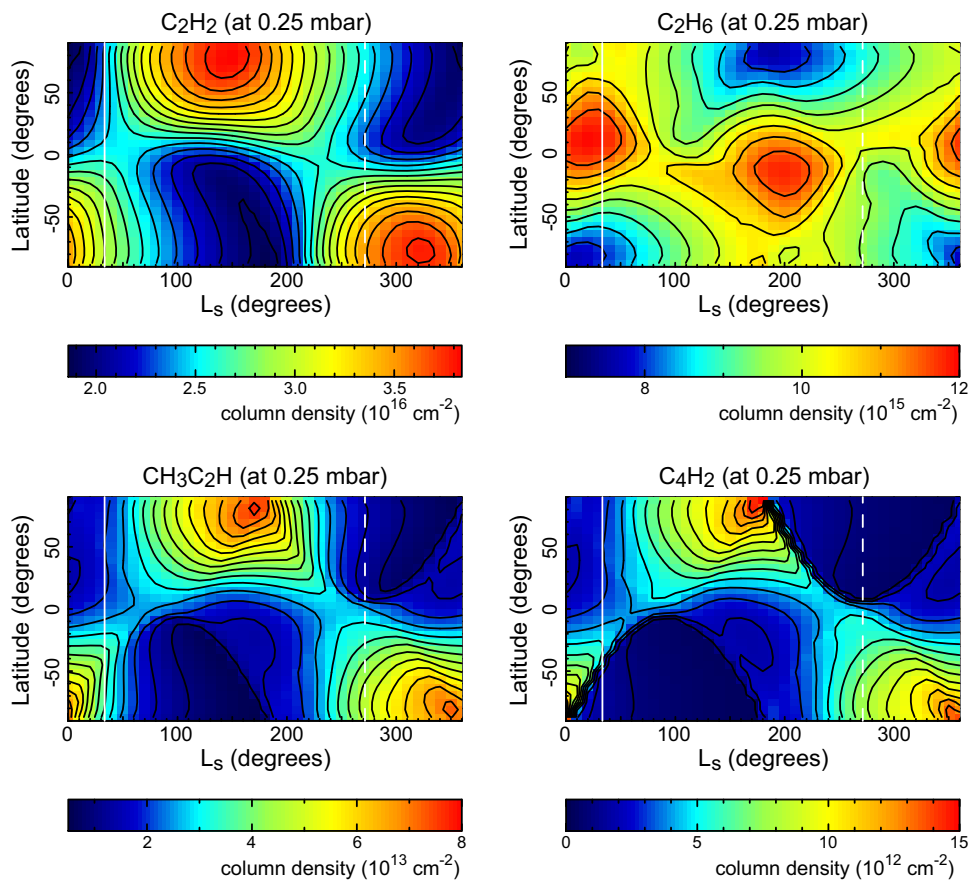
Figure 18: The column abundance of acetylene (Top left), ethane (Top right), methylacetylene (Bottom left), and diacetylene (Bottom right) on Uranus above 0.25 mbar, as a function of planetocentric latitude and season (L_s). The dashed vertical line represents the time of the *Voyager* encounter, and the solid vertical line represents the next Uranus opposition on 24 October 2018.

The abundance of diacetylene is particularly sensitive to solar irradiation. Because the C_4H_2 chemical lifetime is short, the diacetylene column density drops precipitously in the winter polar night once the sun drops below the horizon, as is obvious in Fig. 18.

As discussed in Section 3.3, C_2H_6 is an exception to the aforementioned

trends in the hydrocarbon distributions with latitude and season. At 0.25 mbar and lower pressures, photolysis effectively destroys C_2H_6, so it survives at these pressures more readily at low latitudes and in the winter-to-spring hemispheres, where the mean daily solar insolation is the lowest.

4. Comparisons with observations

Low signal-to-noise ratios prevented mapping of the hydrocarbon infrared emission features during the *Voyager* flybys of Uranus and Neptune, so no measurements of photochemical product abundances as a function of latitude were ever reported from the only spacecraft to ever encounter these planets. The large heliocentric distances and cold atmospheric temperatures of Uranus and Neptune also pose challenges for obtaining spatially resolved observations of hydrocarbon photochemical products from Earth-based telescopes. Hammel et al. (2007) and Orton et al. (2007) were the first to show spatially resolved images of C_2H_6 emission on Neptune, and Greathouse et al. (2011) were the first to present meridional distributions of C_2H_2 and C_2H_6. Greathouse et al. (2011) used the TEXES spectrograph at the Gemini North 8-m telescope in October 2007 (Neptune $L_s = 275.4°$) to obtain high-spectral-resolution, spatially resolved observations of emission from H_2, CH_4, C_2H_2, and C_2H_6 at thermal-infrared wavelengths. Emission from the S(1) rotational line of H_2 and the ν_4 band of CH_4 were used to constrain stratospheric temperature fields, which then allowed Greathouse et al. (2011) to retrieve ethane and acetylene mixing ratios as a function of pressure and latitude. Their results at the peak of the contribution functions from the strong mid-IR C_2H_2 and C_2H_6 lines are shown in Fig. 19, in comparison with our results

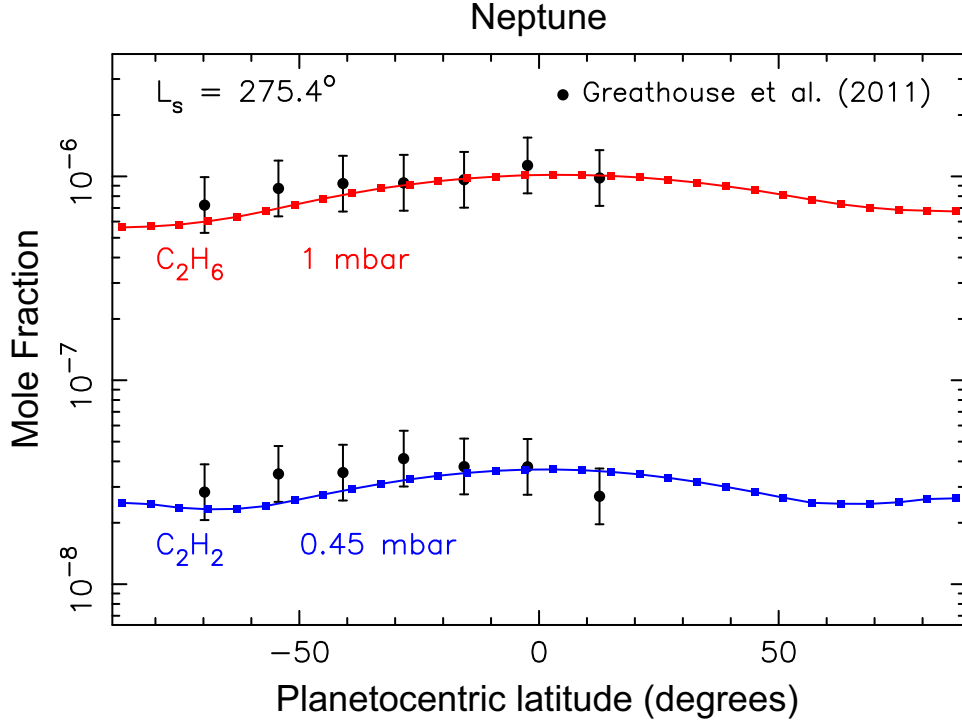at $L_s = 280°$ for the same pressure levels.

Neptune

Figure 19: Model predictions for the meridional variation of the ethane mixing ratio at 1 mbar (red curve) and the acetylene mixing ratio at 0.45 mbar (blue curve) at $L_s = 280°$, in comparison with the retrievals of Greathouse et al. (2011) from Gemini/TEXES observations at $L_s = 275.4°$.

Our seasonal photochemical model provides an excellent fit to the Greathouse et al. (2011) retrieved meridional distribution of C_2H_6 at 1 mbar, with both model and data exhibiting a peak mixing ratio at the equator that then drops off gradually toward higher latitudes in both hemispheres. For acetylene, the observations indicate a slight maximum in the C_2H_2 mixing ratio at $-28°$ latitude, with mixing ratios dropping gradually toward both lower and higher latitudes. This C_2H_2 meridional behavior is not predicted by the models,

which instead exhibit an equatorial maximum mixing ratio with more-or-less symmetric behavior across the equator at this season (Fig. 19), and a column abundance above 1 mbar that peaks at $-9°$ latitude (see Fig. 14). However, the C_2H_2 meridional distribution from the model, as well as an ad hoc constant-with-latitude distribution, are both consistent with the retrievals to within observational uncertainties. This model-data consistency for Neptune hydrocarbon distributions is in sharp contrast to similar comparisons for Jupiter (Liang et al., 2005; Nixon et al., 2007, 2010; Zhang et al., 2013; Fletcher et al., 2016) and Saturn (Moses and Greathouse, 2005; Guerlet et al., 2009, 2010; Friedson and Moses, 2012; Sinclair et al., 2013, 2014; Sylvestre et al., 2015; Hue et al., 2015), for which stratospheric circulation and/or other meridional/vertical transport processes have been suggested as influencing the large-scale meridional hydrocarbon distributions. The good model-data comparisons here for Neptune suggest that either stratospheric winds are weaker and have less of an effect on hydrocarbon distributions on Neptune, or that degeneracies in retrievals and/or uncertainties in models and their related assumptions are resulting in a fortuitous coincidence.

Spatially resolved observations of C_2H_6 on Neptune from two different mid-infrared observational data sets (Keck/LWS spectra from 2003 and Gemini-S/TReCS spectra from August 2007) were also presented by Fletcher et al. (2014). A factor of $\sim$2 difference in the meridionally averaged 1-mbar C_2H_6 mixing ratio between the two data sets highlights the difficulties inherent in calibrating mid-infrared ground-based spectra and suggests that degeneracies between temperatures and abundances are a perennial issue for the retrievals, particularly when dealing with low-resolution spectra. Fletcher et al. (2014)

also point to poor weather conditions and the lack of a Cohen standard star for calibration of the 2007 Gemini-S spectra. The Fletcher et al. retrievals of the Keck data from 2003 exhibit a maximum in the 1-mbar C_2H_6 abundance at the equator, declining gradually toward higher latitudes — consistent with both our photochemical models and the retrievals of Greathouse et al. (2011). The Fletcher et al. retrievals from the Gemini-S data from 2007 have a higher overall C_2H_6 mixing ratio and fine-scale meridional structure, including a local minimum at the equator and the south pole, that are not consistent the photochemical models or with the retrievals of Greathouse et al. (2011). Fletcher et al. (2014) suggest that differences between the 2003 and 2007 data sets are caused by either poor weather for the 2007 observations, calibration issues, or by changes in lower-stratospheric temperatures that are not sampled reliably in retrievals of low-resolution spectra.

From the time of the *Voyager* encounter with Neptune in 1989 to the 2007 observations of Greathouse et al. (2011) and Fletcher et al. (2014), the southern hemisphere of Neptune had swung more prominently into view from the Earth, and our models suggest that the overall column abundance of C_2H_6 above 1 mbar would have been increasing over that time period in the southern hemisphere. This trend is superficially consistent with the report of Hammel et al. (2006) of an increase in global-average ethane emission over the time period from 1985 to 2003. On the other hand, Hammel et al. (2006) observe a decrease in emission from 2003 to 2004 that is not consistent with the photochemical models, and Fletcher et al. (2014) argue for a possible slight decrease in the global-average C_2H_6 mixing ratio from 2003 to mid-2007, with a sharper increase in late 2007, none of which are predicted

by the models. The hydrocarbon emission depends on both atmospheric temperatures and abundances, and it remains to be seen whether the photochemical model predictions are consistent with the observed time-variable trends and/or whether other factors such as adiabatic heating/cooling and variations in abundances due to transport effects are in play.

No retrievals of hydrocarbon abundances as a function of latitude have ever been published for Uranus. The stratosphere of Uranus is colder than that of Neptune, and detecting any hydrocarbon emission other than from CH_4 and C_2H_2 from Earth-based telescopes has typically been difficult. The *Voyager* encounter with Uranus in 1986 occurred near southern summer solstice. Analyses of the ultraviolet solar occultation during the *Voyager* encounter yielded C_2H_2 and C_2H_6 vertical profiles near the equatorial region (Herbert et al., 1987; Bishop et al., 1990). The peak C_2H_2 mixing ratio derived from this UV occultation is less than that derived from global-average *Infrared Space Observatory* (ISO) observations obtained in 1996 (Encrenaz et al., 1998). Because the southern hemisphere of Uranus was still dominating the whole-disk observations in 1996, our photochemical model predictions for enhanced southern hemispheric C_2H_2 during this time period are qualitatively consistent with the greater C_2H_2 abundance seen by Encrenaz et al. (1998), in comparison with the equatorial region during the *Voyager* encounter (see Fig. 18).

Later *Spitzer*/IRS observations of Uranus acquired near the 2007 equinox suggest a very slight decrease in the C_2H_2 abundance in comparison with the Encrenaz et al. (1998) ISO observations. This result, too, appears qualitatively consistent with the models, as the emission from the predicted greater

47

abundance of C_2H_2 in the southern hemisphere would still be dominating the whole-disk observations at the equinox (Fig. 18), and the hemispheric-averaged C_2H_2 column abundance decreased between 1998 and 2007 in the model. The models predict a continued decrease in the C_2H_2 abundance in the southern hemisphere over the next few years, accompanied by an increase in the northern hemisphere abundance.

5. Implications for future observations and modeling

Large ground-based telescopes are currently capable of spatially resolving Uranus and Neptune at mid-infrared wavelengths (e.g., Greathouse et al., 2011; Fletcher et al., 2014; Orton et al., 2014a), and our models provide hypotheses for the distribution of hydrocarbons that can be tested with such future observations. In addition, the *James Webb Space Telescope* (JWST), which is due to be operational shortly (currently delayed launch date March-to-June, 2019), will be able to provide spatially-resolved spectroscopic maps of Uranus and Neptune. Of particular interest onboard JWST is the Medium Resolution Spectrometer (MRS) of the MIRI instrument (Rieke et al., 2015), an Integral Field Unit (IFU) with the capability to provide spatially-resolved 5-28 μm spectroscopy across the planetary disks (Norwood et al., 2016). The resulting spectral maps will provide key observational tests of the two-dimensional hydrocarbon distributions predicted by our models.

We use the time-, latitude- and altitude-dependent hydrocarbon profiles from our models to simulate the expected spectral radiance and brightness temperatures that could be observed by the MIRI instrument. Our assumed spatially-uniform stratospheric temperatures were combined with the two-

dimensional (latitude, altitude) tropospheric temperatures as measured by Voyager-2/IRIS (Orton et al., 2015; Fletcher et al., 2014) to provide a realistic estimate of the temperature distribution, although we note that stratospheric temperature contrasts, if present, would significantly alter our results. We employ the NEMESIS optimal estimation retrieval algorithm (Irwin et al., 2008) in forward-modelling mode, simulating the top-of-atmosphere spectral radiance for all pixels on the observable disk, accounting for the latitude, longitude, and emission angle of the individual pixel element. The spatial orientation and size of each disk was calculated for their 2018 oppositions (3.7" for Uranus on October 24th; 2.4" for Neptune on September 7th). The launch delay to 2019 will not have a significant effect on these simulations, given the long seasonal timescales of both worlds. However, JWST is only capable of observing during a limited range of solar elongations, such that the planets will be observed closer to quadrature with a slightly degraded spatial resolution (angular diameter 3.6" for Uranus, 2.3" for Neptune).

The MIRI forward-model simulations include both collision-induced continuum emission from H_2-H_2, H_2-He and H_2-CH_4, as well as emission and absorption from the gaseous species in our photochemical model. Sources of spectral line data are described in Fletcher et al. (2014) and were used to generate k-distributions (absorption coefficients ranked in order of strength on a wavelength, temperature, and pressure grid) for use in NEMESIS. These k-distributions were generated for CH_4 and its isotopologues, C_2H_2, C_2H_4, C_2H_6, C_3H_4, C_3H_8, C_4H_2, CO_2 and C_6H_6. The tables covered each of the 12 sub-bands (i.e., four IFUs with three subbands each) of MIRI between 5-28 μm, using the correct variation of the spectral resolution ($R \sim 1550 - 3250$)

with wavelength. The four IFUs have fields of view ranging from 3.9" at the shortest wavelength to 7.7" at the longest wavelength, easily accommodating the disks of Uranus and Neptune. However, as the detector pixel scales (variable from 0.196" to 0.273") and image slicer scales (variable from 0.176" to 0.645") undersample the spectral line spread function and spatial point spread functions (diffraction limited spatial resolution 0.19" at 4.89 μm to 1.10" at 28.45 μm), respectively, and as the MIRI consortium is implementing dithering techniques to optimize sampling of the target field, we elected to base our simulation on the 0.11"/pixel plate scale of the MIRI imager, combined with the diffraction-limited performance of the 6.5-m mirror. This plate scale significantly oversamples the FWHM of JWST's primary mirror and is smaller than the best plate scale of the MIRI IFU, but it is representative of the expected noise-free quality with an optimal use of telescope dithering.

Disk images at every wavelength were convolved with a Gaussian, representing the diffraction-limited spatial resolution of a 6.5-m primary mirror, and then averaged spectrally to highlight interesting hydrocarbon features. Finally, a brightness-temperature cross section was extracted along the central meridian (to show meridional variations) and along a latitude circle at the sub-Earth latitude (to show the variation of brightness temperature with emission angle).
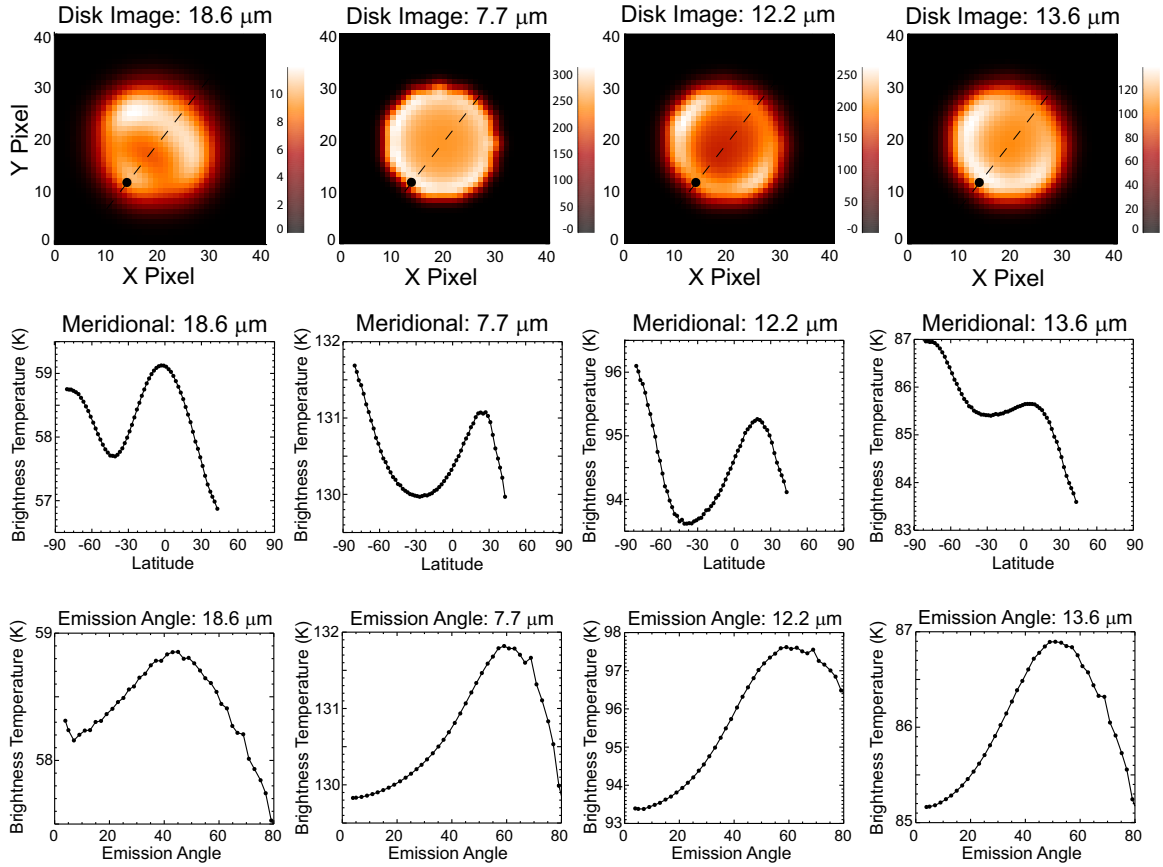
Figure 20: Synthetic images of Neptune (Top row) relevant to the next opposition on 7 September 2018, simulating what the JWST MIRI instrument would be able to see if it were operating at that time: (Left) in the tropospheric continuum at 18.6 μm, (Second from left) in the methane emission band at 7.7 μm, (Second from right) in ethane emission at 12.2 μm, and (Right) in acetylene emission at 13.6 μm. The dashed line marks the central meridian, and the black dot is at the position of the south pole. Brightness-temperature cross sections in the same four wavelength regions were also extracted (Middle row) along the central meridian to highlight latitude variations and (Bottom row) along a latitude circle at the sub-Earth latitude to highlight variations in brightness temperature with emission angle.
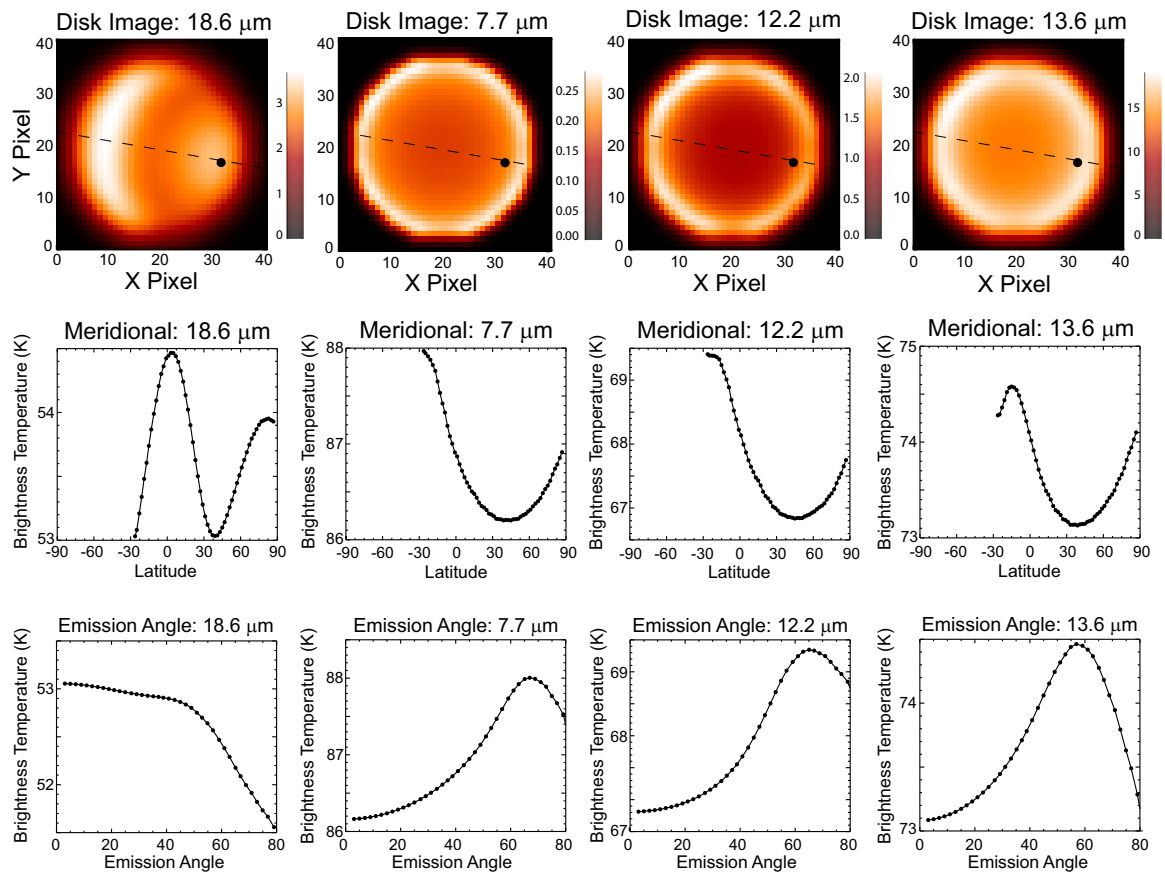
51

Figure 21: Same as Figure 20, except for Uranus at the next opposition on 24 October 2018, and the black dot is at the north pole.

Figure 20 shows the simulated MIRI images for Neptune. The tropospheric temperature structure is probed at 18.6 μm. The assumed Voyager-era thermal structure (Conrath et al., 1998; Fletcher et al., 2014), with broad mid-latitude temperature minima sandwiched between warmer equatorial and high-latitude regions — which was assumed for these synthetic images but was not considered in the photochemical models — shows up readily in the 18.6 μm images. For a lack of information to the contrary, we have assumed a uniform stratospheric thermal structure and spatially uniform eddy diffusion coefficients in both the photochemical model and synthetic images, which result in roughly uniform methane vertical profiles across the planet. The images in methane emission at 7.7 μm are therefore relatively bland, with limb brightening dominating the observed emission. If any latitudinally variable stratospheric temperatures are actually present on Neptune, these should show up readily in all the hydrocarbon emission bands. Limb brightening is also apparent in the ethane emission at 12.2 μm and acetylene emission at 13.6 μm, but the meridional emission cross sections also show evidence for the predicted compositional gradients. For example, the 1-mbar low-latitude column-density maximum in C_2H_6 during this season (see Fig. 13) enhances the low-latitude emission at 12.2 μm, while the strong enhancement in the stratospheric column abundance on C_2H_2 at high southern latitudes is readily apparent in the 13.6 μm images.

Figure 21 shows the simulated MIRI images for Uranus. As with Neptune, the Voyager-derived tropospheric thermal structure shows a temperature minimum at mid-latitudes (Flasar et al., 1987; Conrath et al., 1998; Orton et al., 2015), which shows up readily in the 18.6 μm images. The as-

53

sumed uniform stratospheric temperature fields lead to rather bland images in the stratospheric emission features, with limb brightening dominating the emission (and note that the brightest emission is not actually right at the limb itself, due to an artifact of the point-spread function of the observatory, convolving dark space with the bright emission from the limb). The compositional gradients are less pronounced on Uranus than on Neptune, so there is in general less structure apparent in the Uranus images at 12.2 and 13.6 μm. Our models predict a greater column abundance of C_2H_6 at low latitudes than high latitudes during this season (see Fig. 18), whereas the C_2H_2 column abundance is more uniform with latitude, and hints of this behavior appear in the 12.2 and 13.6 μm cross sections, respectively, although any thermal contrasts in the stratosphere as a function of latitude would likely obscure these differences in the real images.

It should be kept in mind that our seasonal photochemical models do not account for changes in stratospheric temperatures with latitude or season, for possible variations in the stratospheric methane profile with latitude or season, or for variations due to the advection of species. Such effects could potentially have a major influence on the hydrocarbon emission profiles and vertical/meridional distributions, with meridional temperature gradients in particular having a likely large effect on the stratospheric emission features seen with MIRI. Future models should add complexity in stages, such as coupling the photochemical model with a radiative model that can accurately predict seasonally variable temperatures, incorporating possible meridional changes in the methane profile, and testing 2D behavior with different zonally average circulation scenarios. Eventually, incorporating simple C_2H_x chem-

istry and realistic hydrocarbon-based radiative transfer into general circulation models would be the ultimate end goal for predictions of the distribution of hydrocarbons as a function of latitude and season on the giant planets.

6. Conclusions

Time-variable photochemical models are used to investigate how hydrocarbon photochemical products vary as a function of altitude, latitude, and season on Uranus and Neptune. The results indicate that meridional and seasonal gradients in hydrocarbon abundances can persist on these planets in the absence of stratospheric circulation.

Based on our theoretical calculations and comparisons with observations, we draw the following conclusions for Neptune:

- Seasonal variations in hydrocarbon abundances on Neptune are predicted to be greater at high latitudes than low latitudes because of the larger seasonal variations in solar insolation at high latitudes.

- The larger mean daily solar insolation in the summer hemisphere leads to greater photochemical production and higher abundances of hydrocarbon photochemical products in the summer hemisphere than the winter hemisphere.

- Seasonal variations in hydrocarbon abundances on Neptune are most pronounced at high altitudes and become progressively weaker at depth because diffusion time constants and chemical lifetimes increase with increasing pressure. Hydrocarbons respond quickly to changes in the solar flux at high altitudes, but the greater time constants at depth

introduce phase lags in the seasonal response to the changing insolation, such that the abundance maxima for long-lived hydrocarbons such as C_2H_2 and C_2H_6 shift to later in the summer season with increasing depth.

- In the absence of advection or other stratospheric transport processes, meridional variations in hydrocarbon abundances will exist on Neptune and will again be greater at high altitudes than low altitudes. At pressures greater than a few mbar, chemical and transport time scales are longer than a Neptune season, and the yearly averaged solar flux then controls the hydrocarbon abundance variation with latitude. Because the yearly average insolation is larger at the equator than the poles at Neptune, most hydrocarbons at pressures greater than a mbar are expected to exhibit abundance maxima at low latitudes, decreasing gradually toward higher latitudes. Hydrocarbons that have short photochemical lifetimes at mbar pressures, such as C_2H_4 and C_4H_2, exhibit additional complicated seasonal behavior.

- Model predictions for the meridional variation of C_2H_2 and C_2H_6 on Neptune compare well with retrievals from the spatially resolved Gemini infrared spectral observations of Greathouse et al. (2011), and the Keck observations of Fletcher et al. (2014) (to within uncertainties of the observational analyses), suggesting that stratospheric circulation is less important in controlling the large-scale hydrocarbon meridional distributions on Neptune than it is on Jupiter and Saturn (cf. Liang et al., 2005; Moses and Greathouse, 2005; Nixon et al., 2007; Guerlet

et al., 2009; Sinclair et al., 2013; Sylvestre et al., 2015; Hue et al., 2015; Fletcher et al., 2016).

Neptune's axial tilt is only a couple degrees greater than that of Saturn, and the predicted seasonal variations on Neptune share many similarities with those on Saturn (cf. Moses and Greathouse, 2005; Hue et al., 2015). Seasonal variations on Uranus, on the other hand, differ notably from both Saturn and Neptune. Although the extreme axial tilt of Uranus is partially responsible for these differences, the very weak atmospheric mixing on Uranus plays a larger role. Our main conclusions with respect to Uranus are the following:

- The weak vertical transport on Uranus confines hydrocarbons to relatively low altitudes. The vertical diffusion time constants and chemical lifetimes tend to be large in the pressure region where the complex hydrocarbons are being produced, which results in more muted seasonal variations on Uranus than on Neptune. Some seasonal variation is expected in the 0.1-1 mbar region of Uranus (leading to notable hemispheric dichotomies in hydrocarbon abundances, with generally greater abundances in the summer-to-fall hemisphere than the winter-to-spring hemisphere), but virtually no seasonal changes are predicted at pressures greater than 1 mbar.

- Most hydrocarbons on Uranus are predicted to have a greater abundance at the poles than the equator, due to the latitude variation of the annual average solar insolation on the highly tilted Uranus. Ethane is an exception to this trend because of effective photolysis loss that can

compete with production; C_2H_6 abundances are on average greater at low latitudes than high latitudes.

Solar Lyman alpha photons scattered from atomic hydrogen in the interplanetary medium provide an important source of photolyzing radiation for both Uranus and Neptune, particularly in the high-latitude polar winter, where sunlight is absent for long periods of time each year. Seasonal variations at high altitudes would be even more significant without this extra UV source.

Based on our photochemical model results, we simulated the emission from Uranus and Neptune that would be observed using the MIRI instrument onboard JWST. We find that hydrocarbon variations with latitude should show up readily in MIRI images of Neptune but would be more muted for Uranus. Keep in mind, however, that the models presented here do not consider possible seasonal variations in stratospheric temperatures, possible latitude variations in the stratospheric methane abundance or its vertical profile, or possible perturbations due to stratospheric circulation, waves, or other transport processes. These factors could potentially play a major role in controlling large-scale vertical and meridional hydrocarbon distributions, particularly on Uranus, where chemical and diffusion time constants are long. Because many of the hydrocarbon photochemical products condense in the cold lower stratospheres of these planets, any (likely) changes in temperature with season could strongly affect the total column density of the condensable products, due to the high sensitivity of the species' vapor pressures to temperatures, although the gas-phase chemistry variations themselves are not very sensitive to temperature (e.g., Moses and Greathouse, 2005; Moses

et al., 2015). Differences in the methane abundance at high versus low latitudes have already been identified in the tropospheres of Uranus and Neptune (Karkoschka and Tomasko, 2009, 2011; Sromovsky et al., 2011, 2014; Irwin et al., 2012; Tice et al., 2013; de Kleer et al., 2015; Luszcz-Cook et al., 2016), and if such differences extend into the stratosphere, would have a major effect on photochemical production rates. Seasonal forcing likely drives stratospheric circulation on Uranus and Neptune (e.g., Flasar et al., 1987; Conrath et al., 1990, 1991a), and could have important consequences for hydrocarbon distributions. The models presented here represent a first-order solution that when compared to observations can provide valuable insights into the physical and chemical processes at play in the stratospheres of Uranus and Neptune. Future 1D, 2D, and 3D models could add complexity, as needed, to explain observations. We present our full model results in the journal supplementary material in the hopes that they will be of use in analyzing future observations, including potential spatially resolved infrared spectral observations from JWST (e.g., Norwood et al., 2016) and potential future spacecraft missions to the ice giants (e.g., Hofstadter et al., 2017; Mousis et al., 2017).

Hydrocarbon photochemical products (both vapor and aerosols) on Uranus and Neptune help control stratospheric heating, cooling, and energy balance, which in turn influence atmospheric dynamics. The gas-phase hydrocarbons reveal the complex chemistry at play in these atmospheres and can act as tracers to illuminate dynamical motions. Furthering our understanding of the three-dimensional time-variable behavior of hydrocarbons on Uranus and Neptune is therefore important for furthering our understanding of the

complex chemical, radiative, and dynamical couplings and feedbacks that characterize our solar-system ice giants.

7. Acknowledgments

References

Allen, M., Yung, Y. L., Waters, J. W., 1981. Vertical transport and photochemistry in the terrestrial mesosphere and lower thermosphere (50-120 km). J. Geophys. Res. 86, 3617–3627.

Atreya, S. K., Ponthieu, J. J., 1983. Photolysis of methane and the ionosphere of Uranus. Planet. Space Sci. 31, 939–944.

Atreya, S. K., Sandel, B. R., Romani, P. N., 1991. Photochemistry and vertical mixing. In: Bergstralh, J. T., Miner, E. D., Matthews, M. S. (Eds.), Uranus. Univ. Arizona Press, Tucson, pp. 110–146.

Bézard, B., Feuchtgruber, H., Moses, J. I., Encrenaz, T., 1998. Detection of methyl radicals (CH$_3$) on Saturn. Astron. Astrophys. 334, L41–L44.

Bézard, B., Romani, P. N., Conrath, B. J., Maguire, W. C., 1991. Hydrocarbons in Neptune's stratosphere from Voyager infrared observations. J. Geophys. Res. 96, 18,961–18,975.

Bézard, B., Romani, P. N., Feuchtgruber, H., Encrenaz, T., 1999. Detection of the methyl radical on Neptune. Astrophys. J. Letters 515, 868–872.

Bishop, J., Atreya, S. K., Herbert, F., Romani, P., 1990. Reanalysis of Voyager 2 UVS occultations at Uranus: Hydrocarbon mixing ratios in the equatorial stratosphere. Icarus 88, 448–464.

Bishop, J., Atreya, S. K., Romani, P. N., Orton, G. S., Sandel, B. R., Yelle, R. V., 1995. The middle and upper atmosphere of Neptune. In: Cruikshank, D. P., Matthews, M. S., Schumann, A. M. (Eds.), Neptune and Triton. Univ. Arizona Press, Tucson, pp. 427–487.

Bishop, J., Atreya, S. K., Romani, P. N., Sandel, B. R., Herbert, F., 1992. Voyager 2 ultraviolet spectrometer solar occultations at Neptune: Constraints on the abundance of methane in the stratosphere. J. Geophys. Res. 97, 11,681–11,694.

Bishop, J., Romani, P. N., Atreya, S. K., 1998. Voyager 2 ultraviolet spectrometer solar occultations at Neptune: Photochemical modeling of the 125–165 nm lightcurves. Planet. Space Sci. 46, 1–20.

Broadfoot, A. L., Atreya, S. K., Bertaux, J. L., Blamont, J. E., Dessler, A. J., Donahue, T. M., Forrester, W. T., Hall, D. T., Herbert, F., Holberg, J. B.,

Hunten, D. M., Krasnopolsky, V. A., Linick, S., Lunine, J. I., Mcconnell, J. C., Moos, H. W., Sandel, B. R., Schneider, N. M., Shemansky, D. E., Smith, G. R., Strobel, D. F., Yelle, R. V., 1989. Ultraviolet spectrometer observations of Neptune and Triton. Science 246, 1459–1466.

Burgdorf, M., Orton, G., van Cleve, J., Meadows, V., Houck, J., 2006. Detection of new hydrocarbons in Uranus' atmosphere by infrared spectroscopy. Icarus 184, 634–637.

Caldwell, J., Wagener, R., Fricke, K.-H., 1988. Observations of Neptune and Uranus below 2000 A with the IUE. Icarus 74, 133–140.

Cavalié, T., Moreno, R., Lellouch, E., Hartogh, P., Venot, O., Orton, G. S., Jarchow, C., Encrenaz, T., Selsis, F., Hersant, F., Fletcher, L. N., 2014. The first submillimeter observation of CO in the stratosphere of Uranus. Astron. Astrophys. 562, A33.

Cavalié, T., Venot, O., Selsis, F., Hersant, F., Hartogh, P., Leconte, J., 2017. Thermochemistry and vertical mixing in the tropospheres of Uranus and Neptune: How convection inhibition can affect the derivation of deep oxygen abundances. Icarus 291, 1–16.

Conrath, B. J., Flasar, F. M., Gierasch, P. J., 1991a. Thermal structure and dynamics of Neptune's atmosphere from Voyager measurements. J. Geophys. Res. 96, 18,931–18,939.

Conrath, B. J., Gautier, D., Lindal, G. F., Samuelson, R. E., Shaffer, W. A., 1991b. The helium abundance of Neptune from Voyager measurements. J. Geophys. Res. 96, 18,907–18,919.

Conrath, B. J., Gierasch, P. J., Leroy, S. S., 1990. Temperature and circulation in the stratosphere of the outer planets. Icarus 83, 255–281.

Conrath, B. J., Gierasch, P. J., Ustinov, E. A., 1998. Thermal structure and para hydrogen fraction on the outer planets from Voyager IRIS measurements. Icarus 135, 501–517.

de Kleer, K., Luszcz-Cook, S., de Pater, I., Ádámkovics, M., Hammel, H. B., 2015. Clouds and aerosols on Uranus: Radiative transfer modeling of spatially-resolved near-infrared Keck spectra. Icarus 256, 120–137.

de Pater, I., Fletcher, L. N., Luszcz-Cook, S., DeBoer, D., Butler, B., Hammel, H. B., Sitko, M. L., Orton, G., Marcus, P. S., 2014. Neptune's global circulation deduced from multi-wavelength observations. Icarus 237, 211–238.

Dobrijevic, M., Cavalié, T., Hébrard, E., Billebaud, F., Hersant, F., Selsis, F., 2010. Key reactions in the photochemistry of hydrocarbons in Neptune's stratosphere. Planet. Space Sci. 58, 1555–1566.

Dobrijevic, M., Ollivier, J. L., Billebaud, F., Brillet, J., Parisot, J. P., 2003. Effect of chemical kinetic uncertainties on photochemical modeling results: Application to Saturn's atmosphere. Astron. Astrophys. 398, 335–344.

Dobrijevic, M., Parisot, J. P., 1998. Effect of chemical kinetics uncertainties on hydrocarbon production in the stratosphere of Neptune. Planet. Space Sci. 46, 491–505.

Encrenaz, T., Combes, M., Atreya, S. K., Romani, P. N., Fricke, K., 1986. A study of the upper atmosphere of Uranus using the IUE. Astron. Astrophys. 162, 317–322.

Encrenaz, T., Feuchtgruber, H., Atreya, S. K., Bezard, B., Lellouch, E., Bishop, J., Edgington, S., Degraauw, T., Griffin, M., Kessler, M. F., 1998. ISO observations of Uranus: The stratospheric distribution of C_2H_2 and the eddy diffusion coefficient. Astron. Astrophys. 333, L43–L46.

Fegley, Jr., B., Prinn, R. G., 1986. Chemical models of the deep atmosphere of Uranus. Astrophys. J. 307, 852–865.

Feuchtgruber, H., Lellouch, E., de Graauw, T., Bézard, B., Encrenaz, T., Griffin, M., 1997. External supply of oxygen to the atmospheres of the giant planets. Nature 389, 159–162.

Feuchtgruber, H., Lellouch, E., Encrenaz, T., Bezard, B., Coustenis, A., Drossart, P., Salama, A., de Graauw, T., Davis, G. R., 1999. Oxygen in the stratospheres of the giant planets and Titan. In: Cox, P., Kessler, M. (Eds.), The Universe as Seen by ISO. Vol. SP-427 of ESA Special Publication. pp. 133–136.

Flasar, F. M., Conrath, B. J., Pirraglia, J. A., Gierasch, P. J., 1987. Voyager infrared observations of Uranus' atmosphere - Thermal structure and dynamics. J. Geophys. Res. 92, 15011–15018.

Fletcher, L. N., de Pater, I., Orton, G. S., Hammel, H. B., Sitko, M. L., Irwin, P. G. J., 2014. Neptune at summer solstice: Zonal mean temperatures from ground-based observations, 2003-2007. Icarus 231, 146–167.

Fletcher, L. N., Drossart, P., Burgdorf, M., Orton, G. S., Encrenaz, T., 2010. Neptune's atmospheric composition from AKARI infrared spectroscopy. Astron. Astrophys. 514, A17.

Fletcher, L. N., Greathouse, T. K., Orton, G. S., Sinclair, J. A., Giles, R. S., Irwin, P. G. J., Encrenaz, T., 2016. Mid-infrared mapping of Jupiter's temperatures, aerosol opacity and chemical distributions with IRTF/TEXES. Icarus 278, 128–161.

Fletcher, L. N., Irwin, P. G. J., Sinclair, J. A., Orton, G. S., Giles, R. S., Hurley, J., Gorius, N., Achterberg, R. K., Hesman, B. E., Bjoraker, G. L., 2015. Seasonal evolution of Saturn's polar temperatures and composition. Icarus 250, 131–153.

Friedson, A. J., Moses, J. I., 2012. General circulation and transport in Saturn's upper troposphere and stratosphere. Icarus 218, 861–875.

Gangopadhyay, P., Izmodenov, V. V., Shemansky, D. E., Gruntman, M., Judge, D. L., 2005. Reappraisal of the Pioneer 10 and Voyager 2 Lyα intensity measurements. Astrophys. J. 628, 514–519.

Giorgini, J. D., Yeomans, D. K., Chamberlin, A. B., Chodas, P. W., Jacobson, R. A., Keesey, M. S., Lieske, J. H., Ostro, S. J., Standish, E. M., Wimberly, R. N., 1996. JPL's on-line solar system data service. In: AAS/Division for Planetary Sciences Meeting Abstracts #28. Vol. 28 of Bulletin of the American Astronomical Society. p. 1158.

Greathouse, T. K., Richter, M., Lacy, J., Moses, J., Orton, G., Encrenaz, T., Hammel, H. B., Jaffe, D., Aug. 2011. A spatially resolved high spectral resolution study of Neptune's stratosphere. Icarus 214, 606–621.

Guerlet, S., Fouchet, T., Bézard, B., Moses, J. I., Fletcher, L. N., Simon-Miller, A. A., Flasar, F. M., 2010. Meridional distribution of CH_3C_2H and C_4H_2 in Saturn's stratosphere from CIRS/Cassini limb and nadir observations. Icarus 209, 682–695.

Guerlet, S., Fouchet, T., Bézard, B., Simon-Miller, A. A., Flasar, F. M., 2009. Vertical and meridional distribution of ethane, acetylene and propane in Saturn's stratosphere from CIRS/Cassini limb observations. Icarus 203, 214–232.

Hammel, H. B., Lynch, D. K., Russell, R. W., Sitko, M. L., Bernstein, L. S., Hewagama, T., Jun. 2006. Mid-Infrared Ethane Emission on Neptune and Uranus. Astrophys. J. Letters 644, 1326–1333.

Hammel, H. B., Sitko, M. L., Lynch, D. K., Orton, G. S., Russell, R. W., Geballe, T. R., de Pater, I., 2007. Distribution of ethane and methane emission on Neptune. Astron. J. 134, 637–641.

Herbert, F., Sandel, B. R., Yelle, R. V., Holberg, J. B., Broadfoot, A. L., Shemansky, D. E., Atreya, S. K., Romani, P. N., 1987. The upper atmosphere of Uranus - EUV occultations observed by Voyager 2. J. Geophys. Res. 92, 15093–15109.

Hesman, B. E., Davis, G. R., Matthews, H. E., Orton, G. S., 2007. The abundance profile of CO in Neptune's atmosphere. Icarus 186, 342–353.

Hofstadter, M., Simon, A., Atreya, S., Banfield, D., Fortney, J., Hayes, A., Hedman, M., Hospodarsky, G., Mandt, K., Masters, A., Showalter, M., Soderlund, K., Turrini, D., Turtle, E. P., Elliott, J., Reh, K., 2017. A vision for ice giant exploration. In: Planetary Science Vision 2050 Workshop. Vol. 1989 of LPI Contributions. p. 8115.

Hue, V., Cavalié, T., *Dobrijevic*, M., Hersant, F., Greathouse, T. K., 2015. 2D photochemical modeling of Saturn's stratosphere. Part I: Seasonal variation of atmospheric composition without meridional transport. Icarus 257, 163–184.

Hue, V., Greathouse, T. K., Cavalié, T., Dobrijevic, M., Hersant, F., 2016. 2D photochemical modeling of Saturn's stratosphere. Part II: Feedback between composition and temperature. Icarus 267, 334–343.

Irwin, P. G. J., Teanby, N. A., Davis, G. R., Fletcher, L. N., Orton, G. S., Calcutt, S. B., Tice, D. S., Hurley, J., 2012. Further seasonal changes in Uranus' cloud structure observed by Gemini-North and UKIRT. Icarus 218, 47–55.

Irwin, P. G. J., Teanby, N. A., de Kok, R., Fletcher, L. N., Howett, C. J. A., Tsang, C. C. C., Wilson, C. F., Calcutt, S. B., Nixon, C. A., Parrish, P. D., 2008. The NEMESIS planetary atmosphere radiative transfer and retrieval tool. Journal of Quantitative Spectroscopy and Radiative Transfer 109, 1136–1150.

Karkoschka, E., Tomasko, M. G., 2009. The haze and methane distributions on Uranus from HST-STIS spectroscopy. Icarus 202, 287–309.

Karkoschka, E., Tomasko, M. G., 2011. The haze and methane distributions on Neptune from HST-STIS spectroscopy. Icarus 211, 780–797.

Kostiuk, T., Romani, P., Espenak, F., Bezard, B., 1992. Stratospheric ethane on Neptune - Comparison of groundbased and Voyager IRIS retrievals. Icarus 99, 353–362.

Lellouch, E., Hartogh, P., Feuchtgruber, H., Vandenbussche, B., de Graauw, T., Moreno, R., Jarchow, C., Cavalié, T., Orton, G., Banaszkiewicz, M., Blecka, M. I., Bockelée-Morvan, D., Crovisier, J., Encrenaz, T., Fulton, T., Küppers, M., Lara, L. M., Lis, D. C., Medvedev, A. S., Rengel, M., Sagawa, H., Swinyard, B., Szutowicz, S., Bensch, F., Bergin, E., Bille-baud, F., Biver, N., Blake, G. A., Blommaert, J. A. D. L., Cernicharo, J., Courtin, R., Davis, G. R., Decin, L., Encrenaz, P., Gonzalez, A., Jehin, E., Kidger, M., Naylor, D., Portyankina, G., Schieder, R., Sidher, S., Thomas, N., de Val-Borro, M., Verdugo, E., Waelkens, C., Walker, H., Aarts, H., Comito, C., Kawamura, J. H., Maestrini, A., Peacocke, T., Teipen, R., Tils, T., Wildeman, K., 2010. First results of Herschel-PACS observations of Neptune. Astron. Astrophys. 518, L152.

Lellouch, E., Moreno, R., Orton, G. S., Feuchtgruber, H., Cavalié, T., Moses, J. I., Hartogh, P., Jarchow, C., Sagawa, H., 2015. New constraints on the CH_4 vertical profile in Uranus and Neptune from Herschel observations. Astron. Astrophys. 579, A121.

Lellouch, E., Moreno, R., Paubert, G., 2005. A dual origin for Neptune's carbon monoxide? Astron. Astrophys. 430, L37–L40.

Lellouch, E., Romani, P. N., Rosenqvist, J., 1994. The vertical Distribution and Origin of HCN in Neptune's Atmosphere. Icarus 108, 112–136.

Liang, M.-C., Shia, R.-L., Lee, A. Y.-T., Allen, M., Friedson, A. J., Yung, Y. L., 2005. Meridional transport in the stratosphere of Jupiter. Astrophys. J. Lett. 635, L177–L180.

Lindal, G. F., Lyons, J. R., Sweetnam, D. N., Eshleman, V. R., Hinson, D. P., 1987. The atmosphere of Uranus - Results of radio occultation measurements with Voyager 2. Journal of Geophysical Research 92, 14987–15001.

Lindal, G. F., Sweetnam, D. N., Eshleman, V. R., 1985. The atmosphere of Saturn: An analysis of the Voyager radio occultation measurements. Astron. J. 90, 1136–1146.

Lodders, K., Fegley, Jr., B., 1994. The origin of carbon monoxide in Neptunes's atmosphere. Icarus 112, 368–375.

Luszcz-Cook, S. H., de Kleer, K., de Pater, I., Adamkovics, M., Hammel, H. B., 2016. Retrieving Neptune's aerosol properties from Keck OSIRIS observations. I. Dark regions. Icarus 276, 52–87.

Luszcz-Cook, S. H., de Pater, I., 2013. Constraining the origins of Neptune's carbon monoxide abundance with CARMA millimeter-wave observations. Icarus 222, 379–400.

Mathis, J. S., Mezger, P. G., Panagia, N., 1983. Interstellar radiation field and dust temperatures in the diffuse interstellar matter and in giant molecular clouds. Astron. Astrophys. 128, 212–229.

Meadows, V. S., Orton, G., Line, M., Liang, M.-C., Yung, Y. L., van Cleve, J., Burgdorf, M. J., 2008. First Spitzer observations of Neptune: Detection of new hydrocarbons. Icarus 197, 585–589.

Moses, J. I., 1992. Meteoroid ablation in Neptune's atmosphere. Icarus 99, 368–383.

Moses, J. I., Allen, M., Yung, Y. L., 1992. Hydrocarbon nucleation and aerosol formation in Neptune's atmosphere. Icarus 99, 318–346.

Moses, J. I., Armstrong, E. S., Fletcher, L. N., Friedson, A. J., Irwin, P. G. J., Sinclair, J. A., Hesman, B. E., 2015. Evolution of stratospheric chemistry in the Saturn storm beacon region. Icarus 261, 149–168.

Moses, J. I., Bézard, B., Lellouch, E., Gladstone, G. R., Feuchtgruber, H., Allen, M., 2000a. Photochemistry of Saturn's atmosphere. I. Hydrocarbon chemistry and comparisons with ISO observations. Icarus 143, 244–298.

Moses, J. I., Fouchet, T., Bézard, B., Gladstone, G. R., Lellouch, E., Feuchtgruber, H., 2005. Photochemistry and diffusion in Jupiter's stratosphere: Constraints from ISO observations and comparisons with other giant planets. J. Geophys. Res. 110, E08001.

Moses, J. I., Greathouse, T. K., 2005. Latitudinal and seasonal models of stratospheric photochemistry on Saturn: Comparison with infrared data from IRTF/TEXES. J. Geophys. Res. 110, E09007.

Moses, J. I., Lellouch, E., Bézard, B., Gladstone, G. R., Feuchtgruber, H., Allen, M., 2000b. Photochemistry of Saturn's atmosphere. II. Effects of an influx of external oxygen. Icarus 145, 166–202.

Moses, J. I., Poppe, A. R., 2017. Dust ablation on the giant planets: Consquences for stratospheric photochemistry. Icarus 297, 33–58.

Moses, J. I., Rages, K., Pollack, J. B., 1995. An analysis of Neptune's stratospheric haze using high-phase-angle Voyager images. Icarus 113, 232–266.

Mousis, O., Atkinson, D. H., Cavalié, T., Fletcher, L. N., Amato, M. J., Aslam, S., Ferri, F., Renard, J.-B., Spilker, T., Venkatapathy, E., Wurz, P., Aplin, K., Coustenis, A., Deleuil, M., Dobrijevic, M., Fouchet, T., Guillot, T., Hartogh, P., Hewagama, T., Hofstadter, M. D., Hue, V., Hueso, R., Lebreton, J.-P., Lellouch, E., Moses, J., Orton, G. S., Pearl, J. C., Sanchez-Lavega, A., Simon, A., Venot, O., Waite, J. H., Achterberg, R. K., Atreya, S., Billebaud, F., Blanc, M., Borget, F., Brugger, B., Charnoz, S., Chiavassa, T., Cottini, V., d'Hendecourt, L., Danger, G., Encrenaz, T., Gorius, N. J. P., Jorda, L., Marty, B., Moreno, R., Morse, A., Nixon, C., Reh, K., Ronnet, T., Schmider, F.-X., Sheridan, S., Sotin, C., Vernazza, P., Villanueva, G. L., 2017. Scientific rationale for Uranus and Neptune in situ explorations. ArXiv e-prints.

Nixon, C. A., Achterberg, R. K., Conrath, B. J., Irwin, P. G. J., Teanby, N. A., Fouchet, T., Parrish, P. D., Romani, P. N., Abbas, M., Leclair, A., Strobel, D., Simon-Miller, A. A., Jennings, D. J., Flasar, F. M., Kunde, V. G., May 2007. Meridional variations of C_2H_2 and C_2H_6 in Jupiter's atmosphere from Cassini CIRS infrared spectra. Icarus 188, 47–71.

Nixon, C. A., Achterberg, R. K., Romani, P. N., Allen, M., Zhang, X., Teanby, N. A., Irwin, P. G. J., Flasar, F. M., 2010. Abundances of Jupiter's

trace hydrocarbons from Voyager and Cassini. Planet. Space Sci. 58, 1667–1680.

Norwood, J., Moses, J., Fletcher, L. N., Orton, G., Irwin, P. G. J., Atreya, S., Rages, K., Cavalié, T., Sánchez-Lavega, A., Hueso, R., Chanover, N., 2016. Giant planet observations with the James Webb Space Telescope. Publications of the Astronomical Society of Pacific 128, 018005.

Orton, G., Encrenaz, T., Leyrat, C., Puetter, R., Friedson, A., 2007. Evidence for methane escape and strong seasonal and dynamical perturbations of Neptune's atmospheric temperatures. Astron. Astrophys. 473, L5–L8.

Orton, G. S., Aitken, D. K., Smith, C., Roche, P. F., Caldwell, J., Snyder, R., 1987. The spectra of Uranus and Neptune at 8-14 and 17-23 microns. Icarus 70, 1–12.

Orton, G. S., Fletcher, L. N., Encrenaz, T., Leyrat, C., Roe, H. G., Fujiyoshi, T., Pantin, E., 2015. Thermal imaging of Uranus: Upper-tropospheric temperatures one season after Voyager. Icarus 260, 94–102.

Orton, G. S., Fletcher, L. N., Moses, J. I., Lellouch, E., Moreno, R., Swinyard, B. M., Hofstadter, M. D., Greathouse, T. K., 2014a. Thermal emission constraints on the atmospheres of Uranus and Neptune. In: Workshop on the Study of the Ice Giant Planets. Vol. 1798 of LPI Contributions. p. 2002.

Orton, G. S., Fletcher, L. N., Moses, J. I., Mainzer, A. K., Hines, D., Hammel, H. B., Martin-Torres, F. J., Burgdorf, M., Merlet, C., Line, M. R., 2014b.

Mid-infrared spectroscopy of Uranus from the Spitzer Infrared Spectrometer: 1. Determination of the mean temperature structure of the upper troposphere and stratosphere. Icarus 243, 494–513.

Orton, G. S., Lacy, J. H., Achtermann, J. M., Parmar, P., Blass, W. E., 1992. Thermal spectroscopy of Neptune: The stratospheric temperature, hydrocarbon abundances, and isotopic ratios. Icarus 100, 541–555.

Orton, G. S., Moses, J. I., Fletcher, L. N., Mainzer, A. K., Hines, D., Hammel, H. B., Martin-Torres, J., Burgdorf, M., Merlet, C., Line, M. R., 2014c. Mid-infrared spectroscopy of Uranus from the Spitzer infrared spectrometer: 2. Determination of the mean composition of the upper troposphere and stratosphere. Icarus 243, 471–493.

Pollack, J. B., Rages, K., Pope, S. K., Tomasko, M. G., Romani, P. N., 1987. Nature of the stratospheric haze on Uranus: Evidence for condensed hydrocarbons. J. Geophys. Res. 92, 15037–15065.

Poppe, A. R., 2016. An improved model for interplanetary dust fluxes in the outer Solar System. Icarus 264, 369–386.

Quémerais, E., Lallement, R., Sandel, B. R., Clarke, J. T., 2009. Interplanetary Lyman α observations: Intensities from Voyagers and line profiles from HST/STIS. Space Science Reviews 143, 151–162.

Rieke, G. H., Wright, G. S., Böker, T., Bouwman, J., Colina, L., Glasse, A., Gordon, K. D., Greene, T. P., Güdel, M., Henning, T., Justtanont, K., Lagage, P.-O., Meixner, M. E., Nørgaard-Nielsen, H.-U., Ray, T. P., Ressler,

M. E., van Dishoeck, E. F., Waelkens, C., 2015. The Mid-Infrared Instrument for the James Webb Space Telescope, I: Introduction. Publications of the Astronomical Society of Pacific 127, 584.

Romani, P. N., Atreya, S. K., 1988. Methane photochemistry and methane production on Neptune. Icarus 74, 424–445.

Romani, P. N., Atreya, S. K., 1989. Stratospheric aerosols from CH_4 photochemistry on Neptune. Geophys. Res. Lett. 16, 941–944.

Romani, P. N., Bishop, J., Bezard, B., Atreya, S., 1993. Methane photochemistry on Neptune: Ethane and acetylene mixing ratios and haze production. Icarus 106, 442–463.

Roques, F., Sicardy, B., French, R. G., Hubbard, W. B., Barucci, A., Bouchet, P., Brahic, A., Gehrels, J.-A., Gehrels, T., Grenier, I., Le Bertre, T., Lecacheux, J., Maillard, J. P., McLaren, R. A., Perrier, C., Vilas, F., Waterworth, M. D., 1994. Neptune's upper stratosphere, 1983-1990: ground-based stellar occultation observations III. Temperature profiles. Astron. Astrophys. 288, 985–1011.

Schulz, B., Encrenaz, T., Bézard, B., Romani, P. N., Lellouch, E., Atreya, S. K., 1999. Detection of C_2H_4 in Neptune from ISO/PHT-S observations. Astron. Astrophys 350, L13–L17.

Sinclair, J. A., Irwin, P. G. J., Fletcher, L. N., Greathouse, T., Guerlet, S., Hurley, J., Merlet, C., 2014. From Voyager-IRIS to Cassini-CIRS: Interannual variability in Saturn's stratosphere? Icarus 233, 281–292.

Sinclair, J. A., Irwin, P. G. J., Fletcher, L. N., Moses, J. I., Greathouse, T. K., Friedson, A. J., Hesman, B., Hurley, J., Merlet, C., 2013. Seasonal variations of temperature, acetylene and ethane in Saturn's atmosphere from 2005 to 2010, as observed by Cassini-CIRS. Icarus 225, 257–271.

Sromovsky, L. A., Fry, P. M., Kim, J. H., 2011. Methane on Uranus: The case for a compact CH_4 cloud layer at low latitudes and a severe CH_4 depletion at high-latitudes based on re-analysis of Voyager occultation measurements and STIS spectroscopy. Icarus 215, 292–312.

Sromovsky, L. A., Karkoschka, E., Fry, P. M., Hammel, H. B., de Pater, I., Rages, K., 2014. Methane depletion in both polar regions of Uranus inferred from HST/STIS and Keck/NIRC2 observations. Icarus 238, 137–155.

Strobel, D. F., Summers, M. E., Herbert, F., Sandel, B. R., 1990. The photochemistry of methane in the atmosphere of Triton. Geophys. Res. Lett. 17, 1729–1731729–17322.

Summers, M. E., Strobel, D. F., 1989. Photochemistry of the atmosphere of Uranus. Astrophys. J. 346, 495–508.

Sylvestre, M., Guerlet, S., Fouchet, T., Spiga, A., Flasar, F. M., Hesman, B., Bjoraker, G. L., 2015. Seasonal changes in Saturn's stratosphere inferred from Cassini/CIRS limb observations. Icarus 258, 224–238.

Teanby, N. A., Irwin, P. G. J., 2013. An external origin for carbon monoxide on Uranus from Herschel/SPIRE? Astrophys. J. Lett. 775, L49.

Tice, D. S., Irwin, P. G. J., Fletcher, L. N., Teanby, N. A., Hurley, J., Orton, G. S., Davis, G. R., 2013. Uranus' cloud particle properties and latitudinal methane variation from IRTF SpeX observations. Icarus 223, 684–698.

Wang, Y., Yelle, R., 1992. Models of the thermal profile of Neptune's upper atmosphere. In: Neptune and Triton Conference Proceedings, January 1992. Tucson, AZ, p. 92.

Woods, T. N., Rottman, G. J., 2002. Solar ultraviolet variability over time periods of aeronomic interest. In: Mendillo, M., Nagy, A., Waite, J. H. (Eds.), Atmospheres in the Solar System: Comparative Aeronomy. Geophysical Monograph Series 130. American Geophysical Union, Washington, DC, pp. 221–233.

Yelle, R. V., Herbert, F., Sandel, B. R., Vervack, Jr., R. J., Wentzel, T. M., 1993. The distribution of hydrocarbons in Neptune's upper atmosphere. Icarus 104, 38–59.

Yelle, R. V., McConnell, J. C., Strobel, D. F., 1989. The far ultraviolet reflection spectrum of Uranus: Results from the Voyager encounter. Icarus 77, 439–456.

Yung, Y. L., Allen, M., Pinto, J. P., 1984. Photochemistry of the atmosphere of Titan: Comparison between model and observations. Astrophys. J. Suppl. 55, 465–506.

Yung, Y. L., DeMore, W. B., 1999. Photochemistry of Planetary Atmospheres. Oxford University Press.

Zhang, X., Shia, R.-L., Yung, Y. L., 2013. Jovian stratosphere as a chemical transport system: Benchmark analytical solutions. Astrophys. J. 767, 172.